Robust and efficient solvers for nonlinear partial differential equations based on random feature method

Longze Tan^{a,c}, Xiaohe Yue^e, Jingrun Chen^{a,b,c,d} and Jiamin Jiang^{b,c,d,*}

ARTICLE INFO

Keywords:

Random feature method

Nonlinear partial differential equa-

tions Nonlinear solvers

Adaptive

Preconditioning

Nonlinear Least Squares Problem

ABSTRACT

Solving nonlinear partial differential equations (PDEs) on complex geometries remains a fundamental yet challenging task in science and engineering. Traditional mesh-based methods often require carefully designed meshes and tailored approximation spaces, leading to high computational cost and implementation difficulties. The random feature method (RFM), a meshfree machine learning-based framework, has emerged as a promising alternative for solving PDEs on complex domains. However, for large three-dimensional nonlinear problems, attaining high accuracy typically requires domain partitioning with many collocation points and random features per subdomain, which leads to extremely large and ill-conditioned nonlinear leastsquares systems. To overcome these challenges, we propose two randomized Newton-type solvers. The first is an inexact Newton method with right preconditioning (IPN), in which randomized Jacobian compression and QR factorization are used to construct an efficient preconditioner that substantially reduces the condition number. Each Newton step is then approximately solved by LSQR, and a derivative-free line search is incorporated to ensure residual reduction and stable convergence. Building upon this framework, we further develop an adaptive multi-step inexact preconditioned Newton method (AMIPN). In this approach, the preconditioned Jacobian is reused across multiple inner iterations, while a prescribed maximum number of inner iterations together with an adaptive early-stopping criterion determines whether the current preconditioner can be retained in subsequent outer iterations. These mechanisms effectively avoid redundant computations and enhance robustness. Extensive numerical experiments confirm the remarkable effectiveness of the proposed solvers. For three-dimensional steady-state PDEs, including elliptic, diffusion-reaction, Helmholtz, and Gray-Scott equations, the methods achieve substantially higher accuracy than classical finite element and finite difference approaches. For two-dimensional time-dependent problems with moving holes, topological changes, large deformations, and complex space-time geometries, the framework demonstrates robust convergence and notable improvements in accuracy. Compared with machine-learningbased solvers such as physics-informed neural networks and weak adversarial networks, our methods consistently yield order-of-magnitude gains, thereby establishing the RFM combined with IPN/AMIPN as an efficient framework for large-scale nonlinear PDEs.

1. Introduction

The numerical solution of nonlinear partial differential equations (PDEs) plays a central role in numerous scientific and engineering applications. However, the problem becomes particularly challenging when the computational domain involves complex geometries, such as those undergoing topological changes, large deformations, or exhibiting intricate structures that render mesh generation infeasible. Classical numerical methods, including the finite difference method (FDM) [1], finite element method (FEM) [2], and spectral method [3], typically rely on carefully constructed approximation spaces and mesh structures tailored to the geometry, both of which require substantial computational effort and manual intervention [4, 5, 6, 7, 8]. In recent years, deep learning-based approaches have emerged as promising alternatives for solving PDEs. Representative examples include physics-informed neural networks (PINNs) [9], the deep Galerkin method (DGM) [10], the weak adversarial networks (WAN) [11], deep Ritz method [12], deep

^aSchool of Mathematical Sciences University of Science and Technology of China Hefei China

 $[^]b$ School of Artificial Intelligence and Data Science University of Science and Technology of China Hefei China

^cSuzhou Institute for Advanced Research University of Science and Technology of China Suzhou China

^dSuzhou Big Data & AI Research and Engineering Center Suzhou China

^eSchool of Mathematical Sciences East China Normal University Shanghai China

^{*}Corresponding author

[≥] ba23001003@mail.ustc.edu.cn (L. Tan); yuexiaohe666@gmail.com (X. Yue); jingrunchen@ustc.edu.cn (J. Chen); jiaminjiang@ustc.edu.cn (J. Jiang)

ORCID(s):

Nitsche method [13], and deep mixed residual method [14], as well as other related approaches. The core idea is to approximate PDE solutions using deep neural networks, with physical laws and prior knowledge embedded in the loss function. These methods are inherently mesh-free, relatively simple to implement, and can flexibly handle irregular boundaries and evolving domains, thereby partially overcoming challenges arising from geometric complexity while also demonstrating notable advantages in tackling high-dimensional problems and inverse modeling tasks [15, 16].

Despite their promising capabilities, deep neural network (DNN)-based methods often exhibit unsatisfactory performance due to the highly nonlinear and nonconvex nature of the underlying optimization problems. The training loss are typically populated with numerous saddle points and sharp local minima, making gradient-based optimization particularly challenging. Common optimizers such as Adam [17] and L-BFGS [18] frequently suffer from vanishing or exploding gradients and often stagnate at an L^2 relative error of about 1% [9, 10, 11], with little improvement even when the network depth or width is increased. As the model size increases, the difficulty of optimization also grows, which may lead to slower convergence and a risk of overfitting. For ill-conditioned or stiff PDEs, these challenges are more pronounced, as the loss are often steep [19], making it difficult for first-order methods to achieve high-accuracy solutions. The training process usually demands considerable time and memory resources and may deliver limited accuracy. Consequently, in many practical problems, current DNN-based PDE solvers have not yet fully reached the performance of traditional numerical methods such as the finite element or finite difference methods in terms of accuracy and efficiency. Nevertheless, DNN solvers demonstrate advantages for handling high-dimensional problems and complex geometries. Enhancing their convergence robustness, training efficiency, and accuracy will be an important direction toward making them practical alternatives in mainstream scientific computing.

In low-dimensional settings, researchers have explored various strategies to integrate traditional numerical methods with machine learning techniques, aiming to leverage the strengths of both approaches [20, 21, 22, 23]. A representative example is the random feature method (RFM) [23], which constructs the global approximation space by combining partition of unity (PoU) with random feature functions. In this framework, random feature functions can be constructed as a two-layer neural network, where the inner-layer parameters are randomly generated and fixed, and only the outputlayer parameters—the coefficients of the random features—are optimized. The PoU functions are typically formed via tensor products of univariate functions. For linear PDEs, the optimization problem associated with the RFM reduces to a convex least-squares system, whereas for nonlinear PDEs it becomes a nonlinear least-squares problem. Consequently, if these systems can be solved efficiently and accurately, the RFM is capable of delivering high-precision solutions without requiring full network training. This property offers an efficient alternative to conventional DNN training, particularly in scientific computing. The RFM has already been successfully applied to a broad spectrum of problems, including solid and fluid mechanics, interface and time-dependent problems, diffusion equations, elliptic eigenvalue problems, and topology optimization [23, 24, 25, 26, 27, 28]. Moreover, the framework has been extended to address more challenging scenarios: for instance, a two-level RFM has been developed by incorporating domain decomposition for elliptic PDEs on geometrically complex domains [29], and an asymptotic-preserving RFM has been proposed by integrating micro-macro decomposition strategies for multiscale radiative transfer equations [30].

In this work, we first introduce the basic framework of the RFM for solving partial differential equations (PDEs). We then observe that when classical nonlinear solvers—such as Newton's method [31], the Levenberg-Marquardt (LM) method [32, 33], Moré's algorithm [34] (as implemented in the MINPACK package), and trust-region (TR) methods [35]—are applied to the large-scale nonlinear least-squares (NLS) problems arising from RFM discretizations of three-dimensional nonlinear PDEs, the main difficulties stem from the fact that the associated Jacobian matrices are often highly ill-conditioned. As a consequence, the linear systems required in the nonlinear iterations can be difficult to solve efficiently and stably at large scales, which may significantly affect the overall convergence performance.

To enable the practical application of the RFM to large-scale nonlinear PDEs, this study proposes two efficient and robust randomized Newton-type solvers. we first propose an inexact Newton method with right preconditioning, where at each iteration the Jacobian is compressed via count sketch, followed by QR factorization to construct a right preconditioner. The preconditioned system is then solved by LSQR, combined with a derivative-free line search to guarantee residual reduction and convergence stability. Secondly, to further accelerate convergence, building upon IPN, we further propose an adaptive multi-step inexact preconditioned Newton method. In this framework, each outer iteration requires only one Jacobian evaluation and preconditioning, and the resulting preconditioned Jacobian can be reused across multiple inner Newton iterations. To avoid redundant computations, the inner loop is assigned a fixed maximum number of inner iterations and equipped with an adaptive early-stopping criterion to determine whether the current preconditioned Jacobian can be reused in the next outer iteration. Moreover, unlike IPN, AMIPN incorporates a

derivative-free line search within the inner loop to ensure residual decrease at every update, thereby further enhancing convergence stability.

Main contributions of this work are summarized as follows:

- We establish the combination of RFM with the proposed IPN/AMIPN solvers as an efficient and robust meshfree computational framework for solving nonlinear PDEs on complex geometries. The proposed nonlinear
 solvers can effectively handle overdetermined and ill-conditioned large-scale systems arising in scientific and
 engineering applications, and provide a potential pathway for the future numerical simulation of complex
 physical processes and coupled problems.
- Comprehensive experiments demonstrate that the solvers achieve accuracy improvements of several orders of
 magnitude compared with finite element, finite difference, and learning-based approaches (PINNs and WANs),
 while maintaining strong robustness and rapid convergence across a broad spectrum of steady-state and timedependent PDEs with complex and evolving geometries.
- To the best of our knowledge, this is the first application of randomized preconditioning techniques to overdetermined large-scale nonlinear systems from neural-network-based discretizations of nonlinear PDEs, thereby constructing efficient and robust nonlinear solvers.

The remainder of this paper is organized as follows. Section 2 introduces the class of nonlinear PDEs under consideration and provides a brief overview of the PINNs and RFM. The convergence limitations of classical nonlinear solvers are illustrated in Section 3 through a representative example. Sections 4 and 5 form the core of the paper: the former presents two new nonlinear solvers, IPN and AMIPN, whereas the latter develops the overall RFM-based framework that incorporates these solvers for the efficient solution of nonlinear PDEs. Section 6 reports numerical results on three-dimensional steady-state and two-dimensional time-dependent problems with complex geometries. Section 7 concludes the paper, and Appendix A provides additional nonlinear examples.

2. Preliminaries

In this section, we first present the mathematical formulation of the nonlinear PDE under consideration, followed by the introduction of the strong-form-based PINNs and RFM.

2.1. The nonlinear PDE problem

We consider the following general nonlinear partial differential equation: find $u:\Omega\to\mathbb{R}$ such that

$$\begin{cases} \mathcal{P}(u(\mathbf{x})) = f(\mathbf{x}), & \mathbf{x} \in \Omega, \\ \mathcal{B}u(\mathbf{x}) = g(\mathbf{x}), & \mathbf{x} \in \partial\Omega. \end{cases}$$
 (2.1)

where $\mathcal{P}(u(\mathbf{x})) = \lambda \mathcal{L}u(\mathbf{x}) + \mu \mathcal{N}(u(\mathbf{x}))$. Here, \mathcal{L} and \mathcal{N} denote a linear and a nonlinear differential operator, respectively; $u(\mathbf{x}) \in \mathbb{R}$ is the unknown field; \mathcal{B} is a (possibly differential or algebraic) boundary operator; f and g are prescribed functions; and $\lambda, \mu \in \mathbb{R}$ are constants. When $\mu = 0$, the problem reduces to a linear one; throughout this work we assume $\mu \neq 0$.

For time-dependent problems we allow $\mathcal L$ to involve temporal derivatives (e.g., ∂_t , ∂_{tt}). We treat time on the same footing as space by augmenting the spatial coordinates with the temporal variable, and regard the problem as d-dimensional with $\mathbf x=(x_1,\dots,x_{d-1},x_d=t)\in\Omega\subset\mathbb R^{d-1}\times[0,T]$ Accordingly, the computational domain Ω encompasses both spatial and temporal dimensions, and the boundary operator $\mathcal B$ encodes not only the spatial boundary conditions on $\partial\Omega\times(0,T]$ but also the initial condition on $\Omega\times\{0\}$, the latter being interpreted as a special type of boundary condition in the spatiotemporal domain.

2.2. Physics-informed neural networks

To solve problem (2.1), the physics-informed neural network is employed to approximate the target solution $u(\mathbf{x})$:

$$u(\mathbf{x}) \approx \hat{u}(\mathbf{x}; \Theta) \triangleq \mathcal{N}(\mathbf{x}; \Theta)$$

where $\mathcal{N}(\mathbf{x}; \Theta)$ denotes a feed-forward neural network with one input layer, L-1 hidden layers, and one output layer, defined as

$$\begin{cases} \mathbf{z}^1 = W^1 \mathbf{x} + \mathbf{b}^1, & \mathbf{h}^1 = \sigma \left(\mathbf{z}^1 \right), \\ \mathbf{z}^l = W^l \mathbf{h}^{l-1} + \mathbf{b}^l, & \mathbf{h}^l = \sigma \left(\mathbf{z}^l \right), & l = 2, 3, \dots, L-1 \\ \mathcal{N}(\mathbf{x}; \Theta) = W^L \mathbf{h}^{L-1} + \mathbf{b}^L, & \end{cases}$$

with $\sigma(\cdot)$ being the nonlinear activation function, and \mathbf{W}^l , \mathbf{b}^l representing the weight matrix and bias vector between the (l-1)-th and l-th layers, respectively. The set of trainable parameters is given by

$$\Theta = \bigcup_{l=1}^{L} \left\{ \mathbf{W}^{l}, \mathbf{b}^{l} \right\}$$

which collects all weights and biases in the network.

The network parameters Θ are obtained by minimizing a physics-informed loss function consistent with the governing equation, defined as

$$\mathcal{L}_{\text{total}}(\hat{u}; \Theta) = \mathcal{L}_{\text{Data}} + \mathcal{L}_{\text{PDE}} + \mathcal{L}_{\text{BC}}$$

where

$$\begin{split} \mathcal{L}_{\mathrm{Data}} &= \lambda_{d} \sum_{i=1}^{N_{d}} \left| \hat{u}\left(\mathbf{x}_{i}; \Theta\right) - u_{i} \right|^{2}, \quad \mathbf{x}_{i} \in \hat{D} \\ \mathcal{L}_{\mathrm{PDE}} &= \lambda_{r} \sum_{i=1}^{N_{\hat{\Omega}}} \left| \mathcal{P}\left(\hat{u}\left(\mathbf{x}_{i}; \Theta\right)\right) - f\left(\mathbf{x}_{i}\right) \right|^{2} = \lambda_{r} \sum_{i=1}^{N_{\hat{\Omega}}} \left| \lambda \mathcal{L} \hat{u}\left(\mathbf{x}_{i}; \Theta\right) + \mu \mathcal{N}\left(\hat{u}\left(\mathbf{x}_{i}; \Theta\right)\right) - f\left(\mathbf{x}_{i}\right) \right|^{2}, \quad \mathbf{x}_{i} \in \hat{\Omega} \\ \mathcal{L}_{\mathrm{BC}} &= \lambda_{b} \sum_{i=1}^{N_{\partial \hat{\Omega}}} \left| \mathcal{B}\left(\hat{u}\left(\mathbf{x}_{i}; \Theta\right)\right) - g\left(\mathbf{x}_{i}\right) \right|^{2}, \quad \mathbf{x}_{i} \in \partial \hat{\Omega} \end{split}$$

Here, \hat{D} is the set of labeled samples of size N_d ; $\hat{\Omega} \subset \Omega$ is the set of collocation points with size $N_{\hat{\Omega}}$; and $\partial \hat{\Omega} \subset \partial \Omega$ is the set of boundary points with size $N_{\partial \hat{\Omega}}$. The coefficients λ_d , λ_r , and λ_b are nonnegative weighting factors that balance the contributions of the data, PDE residual, and boundary condition terms, respectively. The differential operators \mathcal{L} and \mathcal{B} are evaluated by means of automatic differentiation. Although PINNs provide a promising framework for solving PDEs, several challenges remain to be addressed: (i) potential imbalances in the multi-objective loss due to scale differences among data, PDE residual, and boundary terms; (ii) possible limitations in accuracy and efficiency resulting from the inherent non-convex optimization, which may lead to convergence to suboptimal solutions; and (iii) a certain reliance on carefully designed architectures or adaptive strategies, which can increase implementation complexity.

2.3. The random feature method

To overcome the limitations of PINNs, single-hidden-layer neural network approaches such as LocELM [22] and RFM have been proposed, in which the hidden-layer parameters are fixed and only the output weights are trained. LocELM, however, often encounters imbalance in problems such as structural mechanics, where the magnitudes of the governing equations and boundary conditions differ substantially, leading to limited accuracy [23]. In contrast, RFM incorporates a rescaling strategy in the loss function to balance the contributions of PDE residuals and boundary/initial conditions, thereby improving both convergence and accuracy.

In RFM, the approximate solution $u_n(\mathbf{x})$ is expressed as a linear combination of n random feature functions defined on Ω , i.e.,

$$u_n(\mathbf{x}) = \sum_{j=1}^n u_j \phi_j(\mathbf{x}). \tag{2.2}$$

While random feature functions are globally defined, solutions to PDEs often exhibit localized variations, potentially at small scales. To capture such behavior, we construct multiple local approximations, each based on an independent random feature model, and blend them seamlessly using partition of unity (PoU) functions.

To construct the PoU, we first introduce a hypercube $\Omega_c = \prod_{i=1}^d \left[a_i,b_i\right]$ of appropriate size that fully contains the domain Ω . Here, $\prod_{i=1}^d \left[a_i,b_i\right]$ denotes the Cartesian product of d intervals, i.e., $\left[a_1,b_1\right] \times \left[a_2,b_2\right] \times \cdots \times \left[a_d,b_d\right]$. The hypercube Ω_c is then partitioned into M_p non-overlapping hyperrectangles $\left\{\Omega_i\right\}_{i=1}^{M_p}$ as $\Omega_c = \bigcup_{i=1}^{M_p} \Omega_i$, $\Omega_i = \prod_{j=1}^d \left[a_{ij},b_{ij}\right]$, with adjacent elements satisfying $a_{i+1,j}=b_{ij}$. This construction is analogous to structured meshing in the finite element method, and can be generalized to more complex partitioning schemes if needed.

Let $\mathbf{x} = (x_1, \dots, x_d)^T \in \Omega$. For each subdomain Ω_i , we introduce the following affine transformation to obtain a partition-dependent normalized coordinate vector $\mathbf{l}_i(\mathbf{x}) = (\tilde{x}_{i1}, \dots, \tilde{x}_{id})^T$:

$$\tilde{x}_{ij} = 2 \frac{x_j - a_{ij}}{b_{ij} - a_{ij}} - 1, \quad i = 1, \dots, M_p, \quad j = 1, \dots, d.$$

Denote the center and half-width (radius) of the hyperrectangle Ω_i as

$$\mu_i = \left(\frac{b_{i1} + a_{i1}}{2}, \dots, \frac{b_{id} + a_{id}}{2}\right)^T, \quad \sigma_i = \left(\frac{b_{i1} - a_{i1}}{2}, \dots, \frac{b_{id} - a_{id}}{2}\right)^T.$$

Using these notations, the transformation can be compactly expressed in vector form as

$$\mathbf{l}_i(\mathbf{x}) = \frac{\mathbf{x} - \boldsymbol{\mu}_i}{\boldsymbol{\sigma}_i}, \quad i = 1, \dots, M_p.$$

This transformation is a simple coordinate scaling and translation that maps the physical subdomain Ω_i bijectively onto the reference hypercube $[-1,1]^d$. Thus, the PoU functions $\{\psi_i(\mathbf{x})\}_{i=1}^M$ are constructed via the tensor product of a univariate function φ :

$$\psi(\mathbf{x}) = \prod_{i=1}^{d} \varphi\left(\tilde{x}_{ij}\right), \quad i = 1, \dots, M_{p}$$

where φ is selected following [23] as

$$\varphi^{a}(y) = \begin{cases} 1, & |y| \le 1, \\ 0, & \text{else,} \end{cases} \quad \text{or} \quad \varphi^{b}(y) = \begin{cases} 1, & |y| \le \frac{3}{4}, \\ \frac{1 - \sin(2\pi|y|)}{2}, & \frac{3}{4} \le |y| \le \frac{5}{4}, \\ 0, & \text{else.} \end{cases}$$
 (2.3)

 $\varphi_a(y)$ is discontinuous with a smaller support, while $\varphi_b(y)$ is continuously differentiable with a larger support. Next, J_i random feature functions on each subdomain Ω_i are constructed as follows

$$\phi_{ij}(\mathbf{x}) = \sigma \left(\mathbf{k}_{ij} \cdot \mathbf{l}_i(\mathbf{x}) + b_{ij} \right), \quad i = 1, \dots, J_i,$$
(2.4)

where the nonlinear activation function σ is often chosen as \tanh or trigonometric functions and each component of \mathbf{k}_{ij} and b_{ij} is chosen uniformly from the interval $\left[-R_{ij},R_{ij}\right]$ and is fixed. The parameter R_{ij} is used to control the initialization range of the weights $\left\{\mathbf{k}_{ij}\right\}$ and $\left\{b_{ij}\right\}$. Thus, the approximate solution $u_n(\mathbf{x})$ can be represented as

$$u_n(\mathbf{x}) = \sum_{i=1}^{M_p} \psi_i(\mathbf{x}) \sum_{i=1}^{J_i} u_{ij} \phi_{ij}(\mathbf{x}),$$
 (2.5)

where u_{ij} $(i = 1, ..., M_p, j = 1, ..., J_i)$ are the unknown coefficients that need to be determined, and $n = (J_1 + ... + J_{M_p})$ denotes the degrees of freedom. A loss function for (2.1) can be formulated as follows

$$Loss = \sum_{\mathbf{x}_{i} \in C_{I}} \sum_{k=1}^{K_{I}} \lambda_{Ii}^{k} \| \mathcal{P}^{k}(u_{n}\left(\mathbf{x}_{i}\right)) - f^{k}\left(\mathbf{x}_{i}\right) \|_{l^{2}}^{2} + \sum_{\mathbf{x}_{i} \in C_{B}} \sum_{\ell=1}^{K_{B}} \lambda_{Bj}^{\ell} \| \mathcal{B}^{\ell}u_{n}\left(\mathbf{x}_{j}\right) - g^{\ell}\left(\mathbf{x}_{j}\right) \|_{l^{2}}^{2}.$$

$$(2.6)$$

Here λ_{Ii}^k and λ_{Bj}^ℓ are penalty parameters, as defined in [23] and $\{\mathbf{x}_i\} \subset \Omega$ and $\{\mathbf{x}_j\} \subset \partial \Omega$ are collocation points. It is worth noting that, when $M_p > 1$ and PoU function $\varphi^a(y)$ is used, smoothness conditions between the adjacent elements in the partition are explicitly imposed by adding regularization terms in loss function (2.6) while no regularization is required when $\varphi^b(y)$ is used for second-order equations due to its first-order continuity. Next, we let K_I and K_B be the number of condition at each interior point and boundary point, respectively. The total number of conditions is $m = K_I \# C_I + K_B \# C_B$. In practice, the coefficients u_{ij} are the only unknown variables in (2.6) when $\mu = 0$. Therefore, the optimization problem (2.6) can be regarded as a NLS problem with respect to u_{ij} .

Remark 2.1. Within the RFM framework, for vector-valued solutions, we approximate each component of the solution individually using (2.5), i.e.,

$$\boldsymbol{u}_n(\mathbf{x}) = \left(u_n^1(\mathbf{x}), \dots, u_n^{K_I}(\mathbf{x})\right)^{\mathsf{T}},$$

where $u_n^q(\mathbf{x}) = \sum_{i=1}^{M_p} \psi_i(\mathbf{x}) \sum_{i=1}^{J_i} u_{ij}^q \phi_{ij}(\mathbf{x}), q = 1, \dots, K_I$, and K_I denotes the output dimension.

3. Classical nonlinear solvers

In this section, we first review several classical nonlinear solvers and then illustrate their numerical results through a three-dimensional nonlinear elliptic PDE example, thereby providing motivation for the methods proposed in this work.

3.1. Nonlinear solvers

Newton's method and the Gauss-Newton method are the most fundamental approaches for solving (2.6), and many efficient NLS algorithms have been developed based on them. Since (2.6) is overdetermined (the number of equations exceeds the number of unknowns), the Newton update at the (k + 1)-th iteration is given by

$$\mathbf{u}_{k+1} = \mathbf{u}_k - \mathbf{J}_k^{\dagger} \mathbf{F}_k, \tag{3.1}$$

where \mathbf{u}_k denotes the k-th iterate, $\mathbf{F}_k = \mathbf{F}(\mathbf{u}_k)$, $\mathbf{J}_k = \mathbf{F}'(\mathbf{u}_k)$ is the Jacobian evaluated at \mathbf{u}_k , and \mathbf{J}_k^{\dagger} is the Moore-Penrose pseudoinverse of \mathbf{J}_k . The iteration (3.1) can be derived from the following linear least-squares problem:

$$\min_{\mathbf{u} \in \mathbb{R}^n} \|\mathbf{F}_k + \mathbf{J}_k(\mathbf{u} - \mathbf{u}_k)\|_2, \tag{3.2}$$

which corresponds to minimizing the residual norm of the first-order Taylor expansion of $\mathbf{F}(\mathbf{u})$ at \mathbf{u}_k . By solving the normal equations corresponding to (3.2), one obtains the Gauss-Newton (GN) method.

The GN method requires the Jacobian J_k at u_k to have full column rank; otherwise the update may be undefined. When J_k is ill-conditioned, the GN step can be excessively long and cause instabilities. To remedy this, Levenberg [32] and Marquardt [33] introduced a nonnegative damping parameter λ_k , yielding the iteration:

$$\mathbf{u}_{k+1} = \mathbf{u}_k - (\mathbf{J}_k^{\mathsf{T}} \mathbf{J}_k + \lambda_k \mathbf{I})^{-1} \mathbf{J}_k^{\mathsf{T}} \mathbf{F}_k.$$

The Levenberg-Marquardt (LM) method is always well defined when $\lambda_k > 0$. Common choices include $\lambda_k = ||\mathbf{F}_k||^2$ [36], which ensures local quadratic convergence but may suffer from numerical difficulties, and $\lambda_k = ||\mathbf{F}_k||$ [37], which alleviates these issues.

Beyond LM-type damping, a representative example is the well-known Moré algorithm [34], which is implemented in the MINPACK software package. Moreover, The LM method can be interpreted as a special case of trust-region

approaches, where the damping parameter implicitly controls the step length instead of updating the trust-region radius explicitly [35, 38].

3.2. Difficulties of classical nonlinear solvers

In this section, we consider a benchmark example to present the numerical results of classical nonlinear solvers, including Newton, LM, Moré, and TR methods, when applied to (2.6). Specifically, we examine the following three-dimensional nonlinear elliptic problem on the unit cube $\Omega = (0, 1)^3$:

$$\begin{cases} -\nabla \cdot (\Lambda(u)\nabla u) = f(x, y, z), & (x, y, z) \in \Omega \\ \Lambda(u) = 1 + u^2 \end{cases}$$
(3.3)

The exact solution is given by

$$u(x, y, z) = (x + y + z)\sin(\pi x)\sin(\pi y)\cos(\pi z)$$

and the corresponding Dirichlet boundary conditions are imposed on $\partial\Omega$.

We uniformly partition Ω along each coordinate direction into N_x , N_y , and N_z subdomains, resulting in $M_p=N_xN_yN_z$ subdomains. Each subdomain is denoted by $\Omega_{e_{mns}}$ with indices $0 \le m \le N_x-1$, $0 \le n \le N_y-1$, and $0 \le s \le N_z-1$, where e_{mns} serves as the subdomain label. On each $\Omega_{e_{mns}}$, collocation points are placed as $(x_p^{e_{mns}}, y_q^{e_{mns}}, z_r^{e_{mns}})$ with $0 \le p \le Q_x-1$, $0 \le q \le Q_y-1$, and $0 \le r \le Q_z-1$, where $x_p^{e_{mns}}, y_q^{e_{mns}}$, and $z_r^{e_{mns}}$ denote sets of Q_x , Q_y , and Q_z points on the respective intervals. With $Q=Q_xQ_yQ_z$ points per subdomain, the total number of interior collocation points is $Q_I=N_xN_yN_zQ$. For problem (3.3), we adopt uniformly spaced collocation points including endpoints. Each subdomain is assigned the same number J of random feature functions. In the numerical experiments, Ω is partitioned into $M_p=8$ subdomains with $N_x=N_y=N_z=2$, collocation points are set with $Q_x=Q_y=Q_z\in\{20,25,30\}$, and the number of random features J is varied as 800, 1200, 1600, and 2000. The PoU function $\psi_i^a(\mathbf{x})$ is employed, the activation function is chosen as t and, and each component of t is independently sampled from the uniform distribution on t in t and t in t is independently sampled from the uniform distribution on t in t in t in t in t is t in t

$$\min_{\mathbf{u} \in \mathbb{R}^n} \|\mathbf{F}(\mathbf{u})\|_2,\tag{3.4}$$

where $\mathbf{F}: \mathbb{R}^n \to \mathbb{R}^m$, with n=8J unknown coefficients and $m=Q_I+Q_b+Q_c$. Here, $Q_b=2(N_xN_yQ_xQ_y+N_xN_zQ_xQ_z+N_yN_zQ_yQ_z)$ corresponds to the number of Dirichlet boundary constraints, and $Q_c=2((N_x-1)N_yN_zQ_yQ_z+(N_y-1)N_xN_zQ_xQ_z+(N_z-1)N_xN_yQ_xQ_y)$ arises from the regularization enforcing smoothness across adjacent subdomains.

All numerical experiments were performed on a computing server equipped with two Intel Xeon Gold 6342 CPUs (48 cores, 96 threads, 2.80 GHz base and 3.50 GHz turbo), 512 GB of RAM, and four NVIDIA A800 GPUs (80 GB memory each, PCIe interface). The implementation was developed in Python 3.10.18 with CUDA 12.2 support, and executed under a 64-bit Linux operating system.

Within this computational environment, we investigate four nonlinear solvers for the NLS problem (3.4): the Newton, LM, Moré, and TR methods. The latter two are implemented in scipy.optimize.least_squares. The numerical results are summarized in Table 1, where "IT" denotes the number of iterations and "CPU" refers to the elapsed CPU time for solving (3.4). The stopping criterion is chosen as $\|\mathbf{J}_k^T\mathbf{F}_k\| < 10^{-6}$, with maximum iterations set to 60 for Newton and 180 for LM. In the implementation, Newton updates the solution using scipy.linalg.lstsq, which calls the LAPACK routine gelsd based on a divide-and-conquer SVD algorithm, whereas LM employs a Cholesky decomposition with the damping parameter chosen as $\lambda_k = \|\mathbf{F}_k\|$ at each iteration. For PDE problems, accuracy is evaluated using the relative L^2 error with respect to the exact solution.

Overall, due to the highly ill-conditioned and large-scale nature of the Jacobian matrices, classical solvers fail to solve the Newton linear systems both efficiently and accurately, leading to pronounced convergence difficulties in this example. In particular, the Moré method did not converge within the 12-hour time limit even for the smallest problem size. As the number of collocation points and basis functions per subdomain increased, the computational costs of Newton, LM, and TR methods grew drastically. Moreover, Newton and LM often failed to converge within the prescribed maximum number of iterations, with their u-errors stagnating at approximately 10^{-4} and 10^{-2} , respectively.

Table 1
Comparison of the Newton and LM methods for the 3D nonlinear elliptic problem (3.3)

(N_x, N_y, N_z)	$\sqrt[3]{Q}$	J	Solver	ΙΤ	CPU	u error	$oldsymbol{H}^1$ error
			Newton	11	1280.39	3.13e - 05	5.11e - 04
	20	800	LM	180	2656.61	1.00e - 01	6.79e - 01
	20		TR	57	6607.49	3.13e - 05	5.11e - 04
			Moré			a	
			Newton	60	7076.28	2.45e - 04	5.41e - 03
		1200	LM	180	7139.62	6.14e - 02	4.59e - 01
(2, 2, 2)	25		TR	55	22745.37	1.32e - 06	2.97e - 05
(2,2,2)		1600	Newton	60	12484.37	2.75e - 04	6.64e - 03
			LM	180	13768.50	5.61e - 02	4.28e - 01
			TR	57	46132.25	1.18e - 07	3.19e - 06
			Newton	60	18426.67	3.37e - 04	7.72e - 03
		1600	LM	180	19728.05	5.01e - 02	3.88e - 01
	30		TR			b	
		2000	Newton LM	60	28162.52	3.53e – 04	8.64e - 03

^a The Moré method in scipy.optimize.least_squares did not converge within the 12-hour time limit, and the computation was therefore terminated.

By contrast, the TR method achieved higher accuracy under certain configurations. For example, when $\sqrt[3]{Q}=25$ with J=1200 and 1600, the relative L^2 errors were 1.32×10^{-6} and 1.18×10^{-7} , respectively—significantly better than the 10^{-4} -level errors obtained by Newton. However, these accuracy gains came at the expense of substantially increased computational cost. For larger-scale systems, the TR method further failed in the underlying SVD routine due to excessive memory requirements.

4. Proposed nonlinear solvers

The results in the previous section indicate that solving the large-scale and highly ill-conditioned NLS problems arising from RFM discretizations of nonlinear PDEs requires the development of efficient and robust solvers. To this end, we propose two randomized Newton-type methods, namely an inexact Newton method with right preconditioning and its adaptive multi-step extension.

4.1. The IPN method

The underlying optimization problem (2.6) can be written as

$$\min_{\mathbf{u} \in \mathbb{R}^n} \|\mathbf{F}(\mathbf{u})\|_2,\tag{4.1}$$

where the k-th Newton correction $\delta \mathbf{u}_k$ is obtained from the linearized system

$$\mathbf{J}(\mathbf{u}_{\nu})\delta\mathbf{u} = -\mathbf{F}(\mathbf{u}_{\nu}),\tag{4.2}$$

with $\mathbf{J}(\mathbf{u}_k) \in \mathbb{R}^{m \times n}$ denoting the Jacobian. For large-scale and ill-conditioned systems, solving (4.2) dominates the overall cost and often deteriorates the convergence of Newton-type methods.

A numerical breakdown was observed when employing the TR method within the scipy.optimize.least_squares routine. Specifically, the underlying LAPACK implementation failed during the SVD step due to excessive memory requirements. The routine reported the following runtime exception: ValueError: Indexing a matrix of 3317760000 elements would incur an integer overflow in LAPACK.

^c The runtime of the LM method exceeds 24 hours, and the iteration is terminated.

To stabilize the iteration, we introduce a right preconditioner \mathbf{R}_{ν}^{-1} and reformulate the Newton system as

$$\mathbf{J}(\mathbf{u}_k)\mathbf{R}_k^{-1}\mathbf{y} = -\mathbf{F}(\mathbf{u}_k), \qquad \delta\mathbf{u} = \mathbf{R}_k^{-1}\mathbf{y}. \tag{4.3}$$

The preconditioner \mathbf{R}_k is constructed such that the preconditioned Jacobian $\tilde{\mathbf{J}}_k = \mathbf{J}(\mathbf{u}_k)\mathbf{R}_k^{-1}$ exhibits a substantially reduced condition number with well-clustered singular values. This ensures fast and stable convergence of Krylov subspace solvers for the inner least-squares problems, thereby enabling efficient and robust Newton iterations.

We employ a randomized sketching strategy to construct \mathbf{R}_{k} : (i) the Jacobian is compressed via count sketch [39, 40, 41].

$$\tilde{\mathbf{B}}_k = \mathbf{S}_k \mathbf{J} \left(\mathbf{u}_k \right), \quad \mathbf{S}_k \in \mathbb{R}^{s \times m}, s = \gamma n, \gamma > 1;$$

(ii) a thin OR factorization is computed as

$$\tilde{\mathbf{B}}_k = \mathbf{Q}_k \mathbf{R}_k, \quad \mathbf{R}_k \in \mathbb{R}^{n \times n}$$

The computation of $\tilde{\mathbf{B}}_k$ requires only $\mathcal{O}(\text{nnz}(\mathbf{J}_k))$ operations, and in practice the count sketch matrix \mathbf{S}_k is never formed explicitly, thereby substantially reducing both memory usage and computational cost.

In summary, the first baseline nonlinear solver, referred to as the IPN method, is outlined in Algorithm 1.

Algorithm 1 IPN method

```
Require: Nonlinear mapping \mathbf{F}(\mathbf{u}), Jacobian \mathbf{J}(\mathbf{u}), initial guess \mathbf{u}_0, oversampling factor \gamma > 1, tolerances \epsilon, \eta
Ensure: approximate solution u
  1: for k = 0, 1, 2, \dots until convergence do
           The preconditioner \mathbf{R}_k is obtained by Count Sketch compression of J(\mathbf{u}_k) to \tilde{\mathbf{B}}_k followed by thin QR
 2:
      factorization.
           Form the preconditioned matrix \tilde{\mathbf{J}}_k = \mathbf{J}(\mathbf{u}_k) \mathbf{R}_k^{-1}.
 3:
           Solve the preconditioned system \min_{\mathbf{y} \in \mathbb{R}^n} \|\tilde{\mathbf{J}}_k \mathbf{y} + \mathbf{F} \left( \mathbf{u}_k \right) \|_2 approximately using LSQR with tolerance \eta.
 4:
```

- Compute the Newton direction $\delta \mathbf{u}_k = \mathbf{R}_k^{-1} \mathbf{y}_k$ Choose $\alpha_k > 0$ by golden-section search such that $\|\mathbf{F}(\mathbf{u}_k + \alpha_k \delta \mathbf{u}_k)\|$ sufficiently decreases. 5:
- 6:
- 7: Set $\mathbf{u}_{k+1} = \mathbf{u}_k + \alpha_k \delta \mathbf{u}_k$. if $|||\mathbf{F}(\mathbf{u}_{k+1})|| - ||\mathbf{F}(\mathbf{u}_k)||| < \varepsilon$ then 8:
- break 9:
- 10: end if
- 11: end for
- 12: **return u** \leftarrow **u**_{k+1}

It was shown in [42] that, under mild assumptions, the preconditioned system satisfies

$$\kappa\left(\tilde{\mathbf{J}}_{k}\right) \leq \sqrt{\frac{1+\epsilon}{1-\epsilon}}, \qquad \epsilon, \delta \in (0,1),$$

with probability at least $1 - \delta$. Importantly, this bound is independent of the condition number $\kappa \left(\mathbf{J}(\mathbf{u}_k) \right)$. Numerical experiments further confirm that the proposed approach significantly improves the singular value distribution, effectively transforming an ill-conditioned system into a well-conditioned one. As a result, the right-preconditioning strategy provides stable and efficient IPN iterations for large-scale NLS problems.

4.2. The AMINP method

In Algorithm 1, the Jacobian matrix is explicitly computed and right-preconditioned at every iteration. However, when the RFM is applied to three-dimensional nonlinear PDEs, the resulting residual system $\mathbf{F}(\mathbf{u})$ is typically very large and structurally complex, making explicit Jacobian construction prohibitively expensive. Numerical experiments further show that the dominant computational cost of the INP method is concentrated in the preconditioning stage. To address this issue, we propose the adaptive multi-step inexact preconditioned Newton method, summarized in Algorithm 2, which requires only one Jacobian evaluation and preconditioning in each outer iteration. The resulting preconditioned Jacobian is reused across multiple approximate Newton steps in the inner loop. In addition, AMIPN prescribes a maximum number of inner iterations together with an adaptive early-stopping criterion to avoid redundant iterations and determine whether the current Jacobian and its preconditioner need to be updated. Moreover, a derivative-free line search is incorporated within the inner loop to ensure monotone residual reduction.

Specifically, at the k-th outer iteration, the first inner step is obtained by

$$\mathbf{d}_{k,0} = \mathbf{R}_{k}^{-1} LSQR \left(\tilde{\mathbf{J}}_{k}, -\mathbf{F}(\mathbf{u}_{k}); \eta \right), \tag{4.4}$$

with the update

$$\mathbf{z}_{k,1} = \mathbf{u}_k + \alpha_0 \mathbf{d}_{k,0}, \quad \mathbf{F}_{k,1} = -\mathbf{F} \left(\mathbf{z}_{k,1} \right),$$

where $\alpha_0 > 0$ is selected by a derivative-free line search to ensure sufficient decrease of the residual norm. Subsequent approximate Newton steps are computed as

$$\mathbf{d}_{k,i} = \mathbf{R}_{k}^{-1} \text{LSQR}\left(\tilde{\mathbf{J}}_{k}, -\mathbf{F}(\mathbf{z}_{k,i}); \eta\right), \quad i = 1, \dots, i_{k} - 1,$$
(4.5)

together with the updates

$$\mathbf{z}_{k,i+1} = \mathbf{z}_{k,i} + \alpha_i \mathbf{d}_{k,i}, \quad \mathbf{F}_{k,i+1} = -\mathbf{F} \left(\mathbf{z}_{k,i+1} \right).$$

The actual number of inner steps i_k is adaptively determined by the early-stopping criterion

$$\|\mathbf{F}_{k,i+1} - \mathbf{F}_{k,i}\| \| < \tau_{\text{rel}} \|\mathbf{F}_{k,0}\|,$$

where $\tau_{\rm rel}$ is a tolerance. If satisfied, the inner loop terminates early and the current preconditioned Jacobian is retained; otherwise, the process continues until the maximum inner iterations $m_{\rm max}$ are reached, after which a new preconditioned Jacobian and preconditioner are recomputed. The resulting trial step of the k-th outer iteration is

$$\mathbf{s}_k = \sum_{i=0}^{i_k - 1} \alpha_i \mathbf{d}_{k,i}.$$

These mechanisms reduce the frequency of Jacobian evaluations and preconditioning, lower the overall computational cost, and preserve robustness and accuracy, thus yielding higher efficiency than IPN for large-scale, ill-conditioned nonlinear least-squares problems from nonlinear PDE discretizations.

Remark 4.1. In Algorithms 1 and 2, employing the golden-section line search offers a substantial advantage in memory efficiency. This approach requires only multiple evaluations of the objective function $\|\mathbf{F}(\mathbf{x}_k + \alpha_k \mathbf{d}_k)\|$ without storing any additional preconditioned matrix. Once the Jacobian \mathbf{J}_k and its preconditioner \mathbf{R} are computed, updates can be applied in place on \mathbf{J}_k to form the preconditioned Jacobian, thereby reducing the memory footprint by nearly half while maintaining comparable search efficiency. This property is particularly beneficial in large-scale computations.

In contrast, using Armijo, Wolfe, or strong Wolfe line searches requires repeatedly accessing \mathbf{J}_k^T and \mathbf{F}_k during each line search at the k-th iteration, which not only increases the computational cost but also necessitates storing both the Jacobian and its preconditioned form, thereby leading to substantially higher memory consumption.

5. RFM equipped with the proposed nonlinear solvers

In this section, we discretize the nonlinear PDE (2.1) using the RFM and combine it with the nonlinear solver introduced in the previous section to develop a complete numerical solution algorithm. The computational domain is defined as $\Omega = \{(x,y,z) \mid x \in [a_1,b_1], y \in [a_2,b_2], z \in [a_3,b_3]\}$. The domain Ω is partitioned—either uniformly or non-uniformly—into N_x , N_y , and N_z subdomains along the x-, y-, and z-directions, respectively, yielding $M_p = N_x N_y N_z$ subdomains in total. Each subdomain is denoted by $\Omega_{e_{mnl}} = [X_m, X_{m+1}] \times [Y_n, Y_{n+1}] \times [Z_l, Z_{l+1}]$, where $0 \le m \le N_x - 1$, $0 \le n \le N_y - 1$, and $0 \le l \le N_z - 1$, and e_{mnl} is the subdomain index. On each subdomain $\Omega_{e_{mnl}}$, collocation points are placed as $(x_p^{e_{mnl}}, y_q^{e_{mnl}}, z_p^{e_{mnl}})$, $0 \le p \le Q_x - 1$, $0 \le q \le Q_y - 1$, $0 \le r \le Q_z - 1$, where

Algorithm 2 Adaptive multi-step inexact right-preconditioned Newton (AMIPN)

Require: $F(\mathbf{u})$, $J(\mathbf{u})$, initial guess \mathbf{x}_0 , tolerances ε (outer) and η (LSQR), maximum outer iterations K, maximum inner steps m_{max} , inner loop early-stopping threshold τ_{rel}

Ensure: approximate solution u

```
1: Form J_0 \leftarrow J(x_0) and perform Steps 2-3 of the IPN method (Algorithm 1) to obtain the preconditioned Jacobian
      \tilde{\mathbf{J}}_0 and the right preconditioner \mathbf{R}_0^{-1}.
 2: for k = 0, 1, ..., K - 1 do
 3:
            Set \mathbf{z}_{k,0} \leftarrow \mathbf{u}_k, \mathbf{F}_{k,0} \leftarrow -\mathbf{F}(\mathbf{u}_k), m_k \leftarrow m_{\text{max}}, FLAG\leftarrow True.
            for i = 0 to m_k - 1 do
 4:
                   Compute the inner direction \mathbf{p}_{k,i} \leftarrow \text{LSQR}(\tilde{\mathbf{J}}_k, \mathbf{F}_{k,i}; \eta).
 5:
                   Compute the inner inexact Newton direction \mathbf{d}_{k,i} \leftarrow \mathbf{R}_{k}^{-1} \mathbf{p}_{k,i}.
 6:
                   choose \alpha_i > 0 by golden-section search such that \|\mathbf{F}(\mathbf{z}_{k,i} + \alpha_i \mathbf{d}_{k,i})\| sufficiently decreases.
 7:
                   update \mathbf{z}_{k,i+1} \leftarrow \mathbf{z}_{k,i} + \alpha_i \mathbf{d}_{k,i} and \mathbf{F}_{k,i+1} \leftarrow -\mathbf{F}(\mathbf{z}_{k,i+1}).
 8:
                  if \|\mathbf{F}_{k,i+1} - \mathbf{F}_{k,i}\| < \tau_{\text{rel}} \|\mathbf{F}_{k,0}\| then
 9:
                         FLAG← False break.
10:
                  end if
11:
            end for
12:
            Update the next iterate as \mathbf{u}_{k+1} \leftarrow \mathbf{z}_{k,i+1} and \mathbf{F}_{k+1} \leftarrow \mathbf{F}(\mathbf{u}_{k+1}).
13:
            if |||\mathbf{F}(\mathbf{u}_{k+1})|| - ||\mathbf{F}(\mathbf{u}_k)||| < \varepsilon then
14:
                   break.
15:
            end if
16:
            if FLAG then
17:
                   Form J_{k+1} \leftarrow J(u_{k+1}) and perform Steps 2-3 of the IPN method (Algorithm 1) to obtain the preconditioned
18:
      Jacobian \tilde{\mathbf{J}}_{k+1} and the right preconditioner \mathbf{R}_{k+1}^{-1}
            end if
19:
20: end for
21: return u \leftarrow u<sub>k+1</sub>.
```

 $x_p^{e_{mnl}}, y_q^{e_{mnl}}, z_r^{e_{mnl}}$ are sets of Q_x, Q_y , and Q_z points distributed on $[X_m, X_{m+1}], [Y_n, Y_{n+1}]$, and $[Z_l, Z_{l+1}]$, respectively. These points can, for example, be uniformly placed within each subinterval including the endpoints.

We employ the affine mapping introduced in Section 2.3 to transform the collocation points on each subdomain $\Omega_{e_{mnl}}$ into the reference cube $[-1,1]^3$. Using the PoU functions $\psi_i^a(\mathbf{x})$ defined in (2.5), the global RFM solution is represented in a piecewise manner over the $N_x N_y N_z$ subdomains. On each subdomain $\Omega_{e_{mnl}}$, the local solution is expressed as a linear combination of J random feature functions, with the same number of basis functions used on all subdomains for consistency. The resulting global approximation takes the form

$$u(x,y,z) = \begin{cases} \sum_{j=1}^{J} \phi_{j}^{000}(x,y,z) \, u_{j}^{000}, & (x,y,z) \in \Omega_{e_{000}}, \\ \sum_{j=1}^{J} \phi_{j}^{001}(x,y,z) \, u_{j}^{001}, & (x,y,z) \in \Omega_{e_{001}}, \\ \vdots & \vdots & \vdots \\ \sum_{j=1}^{J} \phi_{j}^{mnl}(x,y,z) \, u_{j}^{mnl}, & (x,y,z) \in \Omega_{e_{mnl}}, \\ \vdots & \vdots & \vdots \\ \sum_{j=1}^{J} \phi_{j}^{N_{x}-1,\,N_{y}-1,\,N_{z}-1}(x,y,z) \, u_{j}^{N_{x}-1,\,N_{y}-1,\,N_{z}-1}, & (x,y,z) \in \Omega_{e_{N_{x}-1,\,N_{y}-1,\,N_{z}-1}}. \end{cases}$$

On each subdomain $\Omega_{e_{mnl}}$, the local approximation takes the form

$$u^{mnl}(x, y, z) = \sum_{i=1}^{J} \phi_j^{mnl}(x, y, z) u_j^{mnl}.$$
 (5.1)

Substituting (5.1) into the governing equation and enforcing it at the collocation point $(x_p^{e_{mnl}}, y_q^{e_{mnl}}, z_r^{e_{mnl}})$ yields

$$\lambda \sum_{j=1}^{J} \left(\mathcal{L} \phi_{j}^{mnl} \right) \Big|_{(x_{p}^{e_{mnl}}, y_{q}^{e_{mnl}}, z_{r}^{e_{mnl}})} u_{j}^{mnl} + \mu \, \mathcal{N} \left(\sum_{j=1}^{J} \phi_{j}^{mnl} u_{j}^{mnl} \right) \Big|_{(x_{p}^{e_{mnl}}, y_{q}^{e_{mnl}}, z_{r}^{e_{mnl}})} = f(x_{p}^{e_{mnl}}, y_{q}^{e_{mnl}}, z_{r}^{e_{mnl}}). \tag{5.2}$$

where $0 \le m \le N_x - 1$, $0 \le n \le N_y - 1$, $0 \le l \le N_z - 1$, $0 \le p \le Q_x - 1$, $0 \le q \le Q_y - 1$, $0 \le r \le Q_z - 1$. We assume that in the nonlinear PDE (2.1), at least one of the operators $\mathcal L$ or $\mathcal N$ is of order k. On the interfaces $x = X_{m+1}$ ($0 \le m \le N_x - 2$), the C^0, \ldots, C^{k-1} continuity reads

$$\begin{cases} \sum_{j=1}^{J} \frac{\partial^{s} \phi_{j}^{mnl}}{\partial x^{s}} \left(X_{m+1}, y_{q}^{mnl}, z_{r}^{mnl} \right) u_{j}^{mnl} - \sum_{j=1}^{J} \frac{\partial^{s} \phi_{j}^{m+1,n,l}}{\partial x^{s}} \left(X_{m+1}, y_{q}^{m+1,n,l}, z_{r}^{m+1,n,l} \right) u_{j}^{m+1,n,l} = 0, \quad s = 0, 1, \dots, k-1, \\ \text{for } 0 \leq m \leq N_{\chi} - 2, \ 0 \leq n \leq N_{\chi} - 1, \ 0 \leq l \leq N_{\chi} - 1, \ 0 \leq q \leq Q_{\chi} - 1, \ 0 \leq r \leq Q_{\chi} - 1. \end{cases}$$
 (5.3)

Similarly, on $y = Y_{n+1}$ $(0 \le n \le N_y - 2)$,

$$\begin{cases} \sum_{j=1}^{J} \frac{\partial^{s} \phi_{j}^{mnl}}{\partial y^{s}} \left(x_{p}^{mnl}, Y_{n+1}, z_{r}^{mnl} \right) u_{j}^{mnl} - \sum_{j=1}^{J} \frac{\partial^{s} \phi_{j}^{m,n+1,l}}{\partial y^{s}} \left(x_{p}^{m,n+1,l}, Y_{n+1}, z_{r}^{m,n+1,l} \right) u_{j}^{m,n+1,l} = 0, \quad s = 0, 1, \dots, k-1, \\ \text{for } 0 \leq m \leq N_{x} - 1, \ 0 \leq n \leq N_{y} - 2, \ 0 \leq l \leq N_{z} - 1, \ 0 \leq p \leq Q_{x} - 1, \ 0 \leq r \leq Q_{z} - 1. \end{cases}$$

On $z = Z_{l+1}$ $(0 \le l \le N_z - 2)$,

$$\begin{cases} \sum_{j=1}^{J} \frac{\partial^{s} \phi_{j}^{mnl}}{\partial z^{s}} \left(x_{p}^{mnl}, y_{q}^{mnl}, Z_{l+1} \right) u_{j}^{mnl} - \sum_{j=1}^{J} \frac{\partial^{s} \phi_{j}^{m,n,l+1}}{\partial z^{s}} \left(x_{p}^{m,n,l+1}, y_{q}^{m,n,l+1}, Z_{l+1} \right) u_{j}^{m,n,l+1} = 0, \quad s = 0, 1, \dots, k-1, \\ \text{for } 0 \leq m \leq N_{\chi} - 1, \ 0 \leq n \leq N_{\chi} - 1, \ 0 \leq l \leq N_{\chi} - 2, \ 0 \leq p \leq Q_{\chi} - 1, \ 0 \leq q \leq Q_{\chi} - 1. \end{cases}$$

$$(5.5)$$

Applying the boundary condition (2.1) to the spatial boundaries $x = a_1, b_1, y = a_2, b_2$, and $z = a_3, b_3$ yields

$$\begin{cases} \sum_{j=1}^{J} \mathcal{B}\Big(\phi_{j}^{mnl}(a_{1},y_{q}^{mnl},z_{r}^{mnl})\Big) u_{j}^{mnl} - g(a_{1},y_{q}^{mnl},z_{r}^{mnl}) = 0, \\ \sum_{j=1}^{J} \mathcal{B}\Big(\phi_{j}^{mnl}(b_{1},y_{q}^{mnl},z_{r}^{mnl})\Big) u_{j}^{mnl} - g(b_{1},y_{q}^{mnl},z_{r}^{mnl}) = 0, \\ \text{for } 0 \leq n \leq N_{y} - 1, \ 0 \leq l \leq N_{z} - 1, \ 0 \leq q \leq Q_{y} - 1, \ 0 \leq r \leq Q_{z} - 1, \ m = 0 \ (x = a_{1}) \ \text{or} \ m = N_{x} - 1 \ (x = b_{1}); \end{cases}$$

$$(5.6)$$

$$\begin{cases} \sum_{j=1}^{J} \mathcal{B}\left(\phi_{j}^{mnl}(x_{p}^{mnl}, a_{2}, z_{r}^{mnl})\right) u_{j}^{mnl} - g(x_{p}^{mnl}, a_{2}, z_{r}^{mnl}) = 0, \\ \sum_{j=1}^{J} \mathcal{B}\left(\phi_{j}^{mnl}(x_{p}^{mnl}, b_{2}, z_{r}^{mnl})\right) u_{j}^{mnl} - g(x_{p}^{mnl}, b_{2}, z_{r}^{mnl}) = 0, \\ \text{for } 0 \leq m \leq N_{x} - 1, \ 0 \leq l \leq N_{z} - 1, \ 0 \leq p \leq Q_{x} - 1, \ 0 \leq r \leq Q_{z} - 1, \ n = 0 (y = a_{2}) \text{ or } n = N_{y} - 1 (y = b_{2}); \end{cases}$$

$$(5.7)$$

$$\begin{cases} \sum_{j=1}^{J} \mathcal{B}\left(\phi_{j}^{mn0}(x_{p}^{mn0}, y_{q}^{mn0}, a_{3})\right) u_{j}^{mn0} - g(x_{p}^{mn0}, y_{q}^{mn0}, a_{3}) = 0, \\ \sum_{j=1}^{J} \mathcal{B}\left(\phi_{j}^{mnl}(x_{p}^{mnl}, y_{q}^{mnl}, b_{3})\right) u_{j}^{mnl} - g(x_{p}^{mnl}, y_{q}^{mnl}, b_{3}) = 0, \\ \text{for } 0 \le m \le N_{x} - 1, \ 0 \le n \le N_{y} - 1, \ 0 \le p \le Q_{x} - 1, \ 0 \le q \le Q_{y} - 1, \ l = 0 (z = a_{3}) \text{ or } l = N_{z} - 1 (z = b_{3}). \end{cases}$$

$$(5.8)$$

Building on the discretization of (2.1), the overall RFM framework—combined with the nonlinear solver, either the INP or AMIPN method—is summarized in the following algorithm.

Algorithm 3 RFM with IPN/AMIPN nonlinear solvers

Require: Partition $\{\Omega_{e_{mnl}}\}$; collocation sets $\{x_p^{e_{mnl}}\}, \{y_q^{e_{mnl}}\}, \{z_r^{e_{mnl}}\}$; basis functions $\{\phi_j^{mnl}\}_{j=1}^J$; operators $\mathcal{L}, \mathcal{N}, \mathcal{B}$; data f, g; continuity order k; initial guess \mathbf{u}_0 ; tolerance ε .

Ensure: Approximate solution.

1: Step 1: Interior assembly. The nonlinear residual of the governing equations, derived from (5.2), is given by

$$\mathbf{R}_{nde}(\mathbf{u}) = \lambda \mathbf{A}_{int} \mathbf{u} + \mu \mathbf{g}_{int}(\mathbf{u}) - \mathbf{f}_{int}.$$

2: Step 2: Continuity assembly. The continuity residual, assembled from (5.3), (5.4), and (5.5), is

$$\mathbf{R}_{con}(\mathbf{u}) = A_{con}\mathbf{u}$$
.

3: Step 3: Boundary conditions. The boundary residual, assembled from (5.6), (5.7), and (5.8), is given by

$$\mathbf{R}_{\mathrm{bdv}}(\mathbf{u}) = \mathbf{A}_{\mathrm{bdv}}\mathbf{u} - \mathbf{b}_{\mathrm{bdv}}.$$

4: Step 4: Global nonlinear system. Define

$$\mathbf{F}(\mathbf{u}) = \begin{bmatrix} \mathbf{R}_{pde}(\mathbf{u}) \\ \mathbf{R}_{con}(\mathbf{u}) \\ \mathbf{R}_{bdv}(\mathbf{u}) \end{bmatrix}, \quad \min_{\mathbf{u}} \frac{1}{2} ||\mathbf{F}(\mathbf{u})||_{2}^{2} \quad \text{equivalently, solve } \mathbf{F}(\mathbf{u}) = 0.$$
 (5.9)

- 5: Step 5: Nonlinear solve. Call the nonlinear solver (Algorithm 1 or Algorithm 2) to solve (5.9).
- 6: **return u**_k, the approximate solution.

Here, A_{int} is obtained by applying the linear operator \mathcal{L} to the random feature basis functions, $g_{int}(u)$ represents the discrete nonlinear contribution, and f_{int} denotes the source term vector. The matrices A_{con} and A_{bdy} correspond to the continuity and boundary constraints, respectively, with **b**bdy denoting the discrete boundary data. The Jacobian of F(u) is then

$$J(\mathbf{u}) = \frac{\partial \mathbf{F}(\mathbf{u})}{\partial \mathbf{u}} = \begin{bmatrix} \lambda \mathbf{A}_{\text{int}} + \mu \frac{\partial \mathbf{g}_{\text{int}}(\mathbf{u})}{\partial \mathbf{u}} \\ \mathbf{A}_{\text{con}} \\ \mathbf{A}_{\text{bdy}} \end{bmatrix}.$$

At the k-th Newton iteration, the correction $\delta \mathbf{u}$ is obtained from the least-squares problem

$$\min_{\delta \mathbf{u} \in \mathbb{D}^n} \|\mathbf{F}(\mathbf{u}_k) + \mathbf{J}(\mathbf{u}_k) \delta \mathbf{u}\|_2. \tag{5.10}$$

Since the PDE, continuity, and boundary contributions may differ significantly in magnitude, the system (5.10) is rescaled before applying IPN or AMIPN. Specifically, the Jacobian $\mathbf{J}_k\left(\mathbf{u}_k\right) = \left(u_{ij}^k\right) \in \mathbb{R}^{m \times n}$, and residual $\mathbf{F}\left(\mathbf{u}_k\right) = \left[f_1\left(\mathbf{u}_k\right), \ldots, f_m\left(\mathbf{u}_k\right)\right]^T \in \mathbb{R}^m$, are scaled row-wise. This procedure follows the idea of adaptive weighting: scaling factors are adjusted according to the magnitude of each residual to prevent any single equation from dominating the iteration, thereby improving numerical comparability and stability.

The scaling factor for the *i*-th row is defined as

$$\lambda_{k,i} = \frac{c}{\max_{1 \le j \le n} |u_{ij}^k|}, \quad i = 1, \dots, m,$$

with c = 100 in all experiments. The scaled system is then

$$u_{ij}^k \leftarrow \lambda_{k,i} u_{ij}^k, \quad f_i \leftarrow \lambda_{k,i} f_i, \quad i = 1, \dots, m, j = 1, \dots, n.$$

After this normalization, the system is successively preconditioned and solved.

6. Numerical experiments

This section presents numerical experiments on two categories of nonlinear PDEs. The first set consists of three-dimensional steady-state problems used to assess the numerical convergence of the RFM combined with the proposed nonlinear solvers, while the second set includes two-dimensional time-dependent problems with complex dynamics or intricate geometries to demonstrate their effectiveness and practicality. The computational environment and notation follow Section 3, with "NJ" denoting the number of Jacobian evaluations. In Algorithms 1 (IPN) and 2 (AMIPN), the sampling factor is fixed at $\gamma = 3$, the LSQR termination tolerance is set to $\eta = 10^{-6}$, and the overall termination tolerance is prescribed as $\varepsilon = 10^{-10}$. For AMIPN, the inner-loop termination criterion is chosen as $\tau_{\rm rel} = 10^{-3}$, and the maximum number of inner steps is set to $m_{\rm max} = 3$.

6.1. Comparison with FEM, FDM, PINN, and WAN

In this section, we evaluate the accuracy of the proposed nonlinear solvers by comparing them with FDM, FEM, PINN, and WAN on the following three-dimensional nonlinear elliptic problem defined on the unit cube domain $(0, 1)^3$:

$$\begin{cases} -\Delta u + u^3 = f(x, y, z), & (x, y, z) \in (0, 1)^3, \\ u(x, y, z) = g(x, y, z), \end{cases}$$
(6.1)

where the exact solution is prescribed as

$$u(x, y, z) = \sin(\pi x)\sin(\pi y)\sin(\pi z).$$

Dirichlet boundary conditions are imposed on $\partial(0,1)^3$.

Table 2
Error comparison of AMIPN, FDM and FEM for solving the 3D nonlinear elliptic equation (6.1).

(N_x, N_y, N_z)	$\sqrt[3]{Q}$	J	Solver	IT	NJ	u error
		400	AMIPN	2	2	5.38e - 05
	20	800	AMIPN	3	2	8.58e - 07
	20		FEM	4		2.80e - 03
			FDM	6		5.19e - 04
(2.2.2)		1200	AMIPN	3	2	3.96e – 08
(2, 2, 2)	25	1600	AMIPN	3	2	3.12e - 09
	25		FEM	4		1.79e – 03
			FDM	6		3.29e - 04
		1600	AMIPN	3	2	3.05e - 09
		2000	AMIPN	3	2	3.66e - 10
	30	2400	AMIPN	3	2	6.20e - 11
			FEM	4		1.25e - 03
			FDM	6		2.27e - 04

Table 2 reports the numerical results of AMIPN, FDM, and FEM, while Figure 1 presents those of PINN and WAN. Both FEM and FDM are performed on uniform grids of sizes 40^3 , 50^3 , and 60^3 . The FEM is implemented using the open-source finite element package FEniCS [43] with standard P_1 Lagrange elements on uniform tetrahedral meshes. For the FDM, a standard second-order central-difference scheme on uniform Cartesian grids is adopted. The resulting nonlinear algebraic systems are solved by Picard iteration with a stopping criterion that the relative change between successive iterates is below 10^{-6} . The PINN employs a fully connected feedforward architecture with five hidden layers of 40 neurons each, whereas the WAN consists of a solution network and an adversarial test network, each with five hidden layers of 50 neurons. The training datasets comprise 18,000 interior points and 6,000 boundary points, both generated via Latin hypercube sampling.

Table 2 shows that, with the same number of collocation points ($\sqrt[3]{Q} = 20, 25, 30$), the AMIPN method produces errors 3–7 orders of magnitude smaller than those of FDM and FEM. The superiority of AMIPN becomes even more evident as both collocation points and basis functions increase. For instance, at $\sqrt[3]{Q} = 25$, the errors of FEM and FDM are approximately 1.79×10^{-3} and 3.29×10^{-4} , while AMIPN achieves only 3.12×10^{-9} with J = 1600. Moreover, for a fixed number of collocation points, enlarging the basis set J yields further accuracy gains: when $\sqrt[3]{Q} = 30$, the error decreases from 3.05×10^{-9} (J = 1600) to 6.20×10^{-11} (J = 2400), demonstrating excellent convergence. Figure 1 confirms this trend, showing that for problem (6.1) the final relative L^2 errors of PINN and WAN remain at $O(10^{-3})$ and $O(10^{-2})$, respectively—several orders of magnitude larger than those of AMIPN.

6.2. Three-dimensional steady nonlinear PDEs

In this section, we consider a set of three-dimensional steady-state partial differential equations—including a strongly nonlinear elliptic equation, a nonlinear diffusion-reaction equation, a nonlinear Helmholtz equation, and the Gray-Scott system—to offer a more comprehensive evaluation of the proposed methods.

To enable a direct comparison with the numerical results in Section 3, we first apply the AMIPN method to the three-dimensional nonlinear elliptic problem (3.3); the results are summarized in Table 3. The table reports the time required to assemble the NLS system via automatic differentiation, the number of outer iterations (IT) and Jacobian evaluations (NJ), the CPU time for solving the NLS system, the final residual norm $\|\mathbf{F}(\mathbf{u}_k)\|_2$, and the relative L^2 and H^1 errors.

With $(N_x, N_y, N_z) = (2, 2, 2)$, increasing $\sqrt[3]{Q}$ and J steadily improves accuracy: the L^2 error decreases from $O(10^{-6})$ to $O(10^{-11})$, the H^1 error from $O(10^{-5})$ to $O(10^{-9})$, and the residual norm from $O(10^{-4})$ to $O(10^{-11})$. Meanwhile, the number of outer iterations stabilizes at five, with four Jacobian evaluations per iteration, whereas the assembly time and CPU time for solving the NLS system increase monotonically with problem size—from about 23 s to 410 s and from 201 s to 2745 s, respectively. These results, together with those in Tables 1 and 3, demonstrate

Table 3
The results of the AMIPN method for the 3D nonlinear elliptic problem (3.3)

(N_x, N_y, N_z)	$\sqrt[3]{Q}$	J	Solver	IT	NJ	Assemble(s)	CPU	$\ \mathbf{F}(\mathbf{u}_k)\ _2$	u error	H^1 error
	20	800	AMIPN	6	4	23.76	201.00	1.07e - 04	1.02e - 06	2.85e - 05
(2, 2, 2)	25	1200 1600	AMIPN AMIPN	5 5	4 4	69.35 117.31	580.62 967.20	3.04e - 06 2.42e - 08	3.87e - 08 3.89e - 09	1.32e - 06 1.48e - 07
	30	1600 2000 2400	AMIPN AMIPN AMIPN	5 5 5	4 4 4	187.94 282.08 410.16	1335.61 2176.57 2744.73	3.96e - 08 5.96e - 10 1.21e - 11	3.41 <i>e</i> - 09 4.16 <i>e</i> - 10 7.04 <i>e</i> - 11	1.30e - 07 $1.77e - 08$ $3.05e - 09$

Table 4
The results of the AMIPN method for the 3D strongly nonlinear elliptic problem (6.2)

(N_x, N_y, N_z)	$\sqrt[3]{Q}$	J	Solver	IT	NJ	$\ \mathbf{F}(\mathbf{u}_k)\ _2$	u error	u_x error	u_y error	u_z error
	20	400 800	AMIPN AMIPN	4 4	3	2.79e - 02 $2.11e - 05$	7.28 <i>e</i> – 05 1.64 <i>e</i> – 06	4.65 <i>e</i> - 04 1.38 <i>e</i> - 05	4.57e - 04 1.67e - 05	1.61 <i>e</i> – 03 5.65 <i>e</i> – 05
(2, 2, 2)	25	1200 1600	AMIPN AMIPN	4 4	3	4.09e - 08 4.83e - 10	5.25e - 08 4.91e - 09	6.02 <i>e</i> - 07 6.11 <i>e</i> - 08	6.00e - 07 6.35e - 08	1.90e – 06 2.28e – 07
	30	1600 2000 2400	AMIPN AMIPN AMIPN	4 4 3	3 3 3	4.57e - 10 1.64e - 11 3.35e - 13	3.73 <i>e</i> - 09 6.47 <i>e</i> - 10 9.33 <i>e</i> - 11	4.84 <i>e</i> - 08 9.13 <i>e</i> - 09 1.44 <i>e</i> - 09	4.75e - 08 9.08e - 09 1.45e - 09	1.65e - 07 $3.21e - 08$ $5.14e - 09$

that the AMIPN method achieves substantially higher accuracy and efficiency than classical solvers such as Newton, LM, Moré, and TR, particularly for large-scale nonlinear elliptic problems.

To further assess the accuracy of the proposed method, we consider the following strongly nonlinear elliptic equation posed on the unit cube $\Omega = (0, 1)^3$:

$$\begin{cases} -\nabla \cdot (\Lambda(\nabla u)\nabla u) = f(x, y, z), & (x, y, z) \in \Omega, \\ u(x, y, z) = g(x, y, z), & (x, y, z) \in \partial\Omega, \end{cases}$$
(6.2)

where $\Lambda(\nabla u) = 1 + |\nabla u|^2$. The exact solution is

$$u(x, y, z) = \sin(x(1-x))\sin(y(1-y))e^{z+1/2},$$

with Dirichlet boundary conditions prescribed on $\partial\Omega$.

Table 4 reports the detailed numerical results for Example (6.2), including the relative L^2 errors of u and its first-order derivatives, the final residual norm $\|\mathbf{F}(\mathbf{u}_k)\|_2$, the number of outer iterations, and the actual number of Jacobian evaluations. As J increases from 400 to 2400, the L^2 error of u decreases from $O(10^{-5})$ to $O(10^{-11})$, and the errors of u_x , u_y , and u_z decrease from $O(10^{-3}-10^{-4})$ to $O(10^{-9})$, exhibiting an approximately exponential convergence trend. These results demonstrate that the AMIPN method achieves extremely high accuracy while converging in only a few iterations, even for this three-dimensional strongly nonlinear elliptic PDE.

To compare the numerical performance of the IPN and AMIPN methods, we consider the following three-dimensional nonlinear Helmholtz equation posed on the unit cube $\Omega = (0, 1)^3$:

$$\begin{cases} u_{xx} + u_{yy} + u_{zz} - 100u + 10\cosh(u) = f(x, y, z), & (x, y, z) \in \Omega, \\ u(x, y, z) = g(x, y, z), & (x, y, z) \in \partial\Omega, \end{cases}$$
(6.3)

Table 5
The results of the IPN and AMIPN methods for the 3D nonlinear Helmholtz equation (6.3)

(N_x, N_y, N_z)	$\sqrt[3]{Q}$	J	Solver	IT	NJ	CPU	Speedup	u error	H^1 error
	20	400	IPN AMIPN	5 3	5 2	52.30 30.21	1.73	$2.55e - 05 \\ 2.54e - 05$	5.85 <i>e</i> - 04 5.83 <i>e</i> - 04
		800	IPN AMIPN	5 3	5 2	170.53 87.87	1.94	4.33e - 07 4.32e - 07	1.31e - 05 1.31e - 05
(2, 2, 2)	2) 25	1200	IPN AMIPN	5 4	5 2	485.91 234.66	2.07	1.91e – 08 1.91e – 08	7.15 <i>e</i> – 07 7.14 <i>e</i> – 07
(2, 2, 2)	23	1600	IPN AMIPN	5 4	5 2	1074.96 437.56	2.40	1.57e - 09 1.57e - 09	6.78e - 08 6.78e - 08
		1600	IPN AMIPN	5 4	5 2	1396.71 593.49	2.35	1.48e - 09 1.47e - 09	6.17e - 08 6.16e - 08
	30		IPN AMIPN	6 4	6 2	2147.64 891.53	2.41	1.91e – 10 9.48e – 09	8.87e - 09 $3.17e - 07$
		2400	IPN AMIPN	6 4	6 2	3386.93 1313.53	2.59	2.64e - 11 2.56e - 11	1.26e – 09 1.26e – 09

with the exact solution

$$u(x, y, z) = (2 + x^2 + y^2 + z^2)\sin(\pi x)\sin(\pi y)\sin(\pi z),$$

and corresponding Dirichlet boundary conditions imposed on $\partial\Omega$.

Table 5 reports the performance of the two solvers for the 3D nonlinear Helmholtz equation. As the numbers of collocation points and random basis functions increase, both methods exhibit markedly improved accuracy: the relative L^2 error decreases from about 10^{-5} at J=400 to 10^{-11} at J=2400, while the H^1 error decreases from $O(10^{-4})$ to $O(10^{-9})$. Notably, AMIPN attains essentially the same accuracy as IPN while requiring fewer outer iterations (3-4 vs. 5-6) and significantly fewer Jacobian evaluations (2 vs. 5-6). Consequently, AMIPN achieves about a $1.7\times$ speedup at smaller problem sizes, which further increases to $2.6\times$ at the largest scale. This trend clearly indicates that the relative advantage of AMIPN over IPN becomes more pronounced as the problem size grows.

We consider the following three-dimensional steady-state nonlinear diffusion–reaction equation posed on the unit ball $\Omega = \{(x, y, z) \in \mathbb{R}^3 : x^2 + y^2 + z^2 \le 1\}$:

$$\begin{cases} -\nabla \cdot (\Lambda(u)\nabla u) + (u^3 - u) + e^u = f(x, y, z), & (x, y, z) \in \Omega, \\ u(x, y, z) = g(x, y, z), & (x, y, z) \in \partial\Omega, \end{cases}$$

$$(6.4)$$

where $\Lambda(u) = 1 + u^2$. The exact solution is chosen as

$$u(x, y, z) = (x^2 + y^2 + z^2)\sin(\pi x)\sin(\pi y)\sin(\pi z),$$

and f(x, y, z) is determined accordingly so that u satisfies (6.4).

The spherical domain is discretized by embedding Ω into the cube $[-1,1]^3$, which is partitioned into $2 \times 2 \times 2$ subdomains. Collocation points are uniformly distributed in each subdomain, and only those with $x^2 + y^2 + z^2 < 1$ are retained to assemble the NLS system. To impose Dirichlet conditions on $\partial\Omega$, 30,000 uniformly distributed boundary points are generated on the unit sphere using the Fibonacci spiral method.

Table 6 reports the numerical results of the AMIPN method. With the subdomain partition fixed at $(N_x, N_y, N_z) = (2, 2, 2)$ and $\sqrt[3]{Q} = 30-35$, increasing the number of random basis functions J from 400 to 2000 leads to substantial accuracy improvement. Specifically, the relative L^2 error of u decreases from 2.21×10^{-4} to 1.51×10^{-9} , while the errors of its first derivatives (u_x, u_y, u_z) decrease from $O(10^{-3}-10^{-4})$ to $O(10^{-8})$. The computational time increases

Table 6Results of the AMIPN method for the 3D 3D steady-state nonlinear diffusion-reaction equation (6.4)

(N_x, N_y, N_z)	$\sqrt[3]{Q}$	J	Solver	IT	NJ	CPU	u error	u_x error	u_y error	u_z error
		400	AMIPN	3	2	83.54	2.21e - 04	1.00e - 03	9.94 <i>e</i> – 04	9.77e – 04
(2, 2, 2)	30	800	AMIPN	3	2	193.29	3.83e - 06	2.42e - 05	2.40e - 05	2.34e - 05
(2, 2, 2)	(2,2,2) 30	1200	AMIPN	3	2	348.00	2.06e - 07	1.53e – 06	1.53e - 06	1.52e – 06
		1600	AMIPN	3	2	616.20	1.62e - 08	1.35e - 07	1.43e - 07	1.35e - 07
	35	2000	AMIPN	3	2	1286.85	1.51e – 09	1.41e - 08	1.41e - 08	1.42e - 08

Table 7Results of the AMIPN method for the 3D steady-state Gray-Scott reaction-diffusion system (6.5)

(N_x, N_y, N_z)	$\sqrt[3]{Q}$	J	Solver	IT	NJ	u error	v error
	20	400	AMIPN	3	2	7.60e - 05	5.00e - 05
	20	800	AMIPN	3	2	1.35e – 06	7.37e - 07
(2, 2, 2)	25	1200	AMIPN	3	2	6.08e - 08	3.71e - 08
		1600	AMIPN	3	2	3.78e - 09	3.13e - 09
	30	1600	AMIPN	4	2	5.01e - 09	2.90e - 09
	20	2000	AMIPN	4	2	4.05e - 10	4.56e - 10

moderately from about 84 s to 1287 s, whereas the numbers of outer iterations and Jacobian evaluations remain fixed at 3 and 2, respectively.

At the end of this section, we consider a larger-scale benchmark problem: the three-dimensional steady-state Gray-Scott reaction-diffusion system posed on the cubic domain $\Omega = (0, 1)^3$:

$$\begin{cases} D_{u}\Delta u - uv^{2} + F(1 - u) = f_{1}(x, y, z), \\ D_{v}\Delta v + uv^{2} - (F + k)v = f_{2}(x, y, z), \end{cases} (x, y, z) \in \Omega,$$
(6.5)

with the exact solution

$$u(x, y, z) = \sin(x(1-x))\sin(y(1-y))e^{z}, \quad v(x, y, z) = \sin(\pi x)\sin(\pi y)\sin(\pi z).$$

In the numerical experiments, we set F=0.060, k=0.062, and use solution-dependent diffusion coefficients $D_u=1+u^2$ and $D_v=1+v^2$. Homogeneous Dirichlet boundary conditions are imposed on $\partial\Omega$. When discretized by the RFM, this coupled system yields a nonlinear least-squares problem whose Jacobian has a dimension approximately twice that of the single-equation problems (6.1)-(6.3).

Table 7 shows that the AMIPN method maintains excellent stability and scalability for this large-scale strongly nonlinear coupled system. As the numbers of collocation points and basis functions increase, the relative errors of u and v decrease from $O(10^{-5})$ to $O(10^{-10})$, exhibiting spectral-like convergence. Convergence is achieved within only 3-4 outer iterations and 2 Jacobian evaluations, highlighting the strong potential of AMIPN for large-scale nonlinear PDE systems.

6.3. Time-dependent nonlinear PDEs on complex evolving domains

Time-dependent PDEs on complex space-time domains pose significant challenges, since they often involve moving boundaries, topological changes, large deformations, and complex geometries. In such scenarios, conventional mesh-based methods typically suffer from severe mesh distortion and frequent remeshing, leading to substantial implementation difficulties, loss of accuracy, and high computational cost.

(N_x, N_y, N_z)	$\sqrt[3]{Q}$	J	Solver	IT	NJ	CPU	u error	u_x error	u_y error	u_t error
	20	400 800	AMIPN AMIPN	3	1 1	22.78 56.50	7.70 <i>e</i> – 05 1.73 <i>e</i> – 06	3.13 <i>e</i> – 04 8.78 <i>e</i> – 06	3.18 <i>e</i> – 04 8.62 <i>e</i> – 06	3.26 <i>e</i> – 03 1.11 <i>e</i> – 04
(2, 2, 2)	25	1200 1600	AMIPN AMIPN	3	1 1	159.11 282.21	5.47e - 08 5.30e - 09	3.59e - 07 3.25e - 08	3.54e - 07 $3.23e - 08$	$4.04e - 06 \\ 5.35e - 07$
	30	1600 2000 2400	AMIPN AMIPN AMIPN	3 3 3	1 1 1	393.06 623.36 1066.48	4.01e - 09 7.25e - 10 1.82e - 10	2.59e - 08 5.22e - 09 8.16e - 10	2.67e - 08 5.30e - 09 7.92e - 10	3.60e - 07 $7.77e - 08$ $1.33e - 08$

Table 8
Results of the AMIPN method for the 2D Allen-Cahn equation (6.6)

Owing to its mesh-free nature, the proposed approach can accurately handle evolving geometries while maintaining high accuracy and numerical stability. To systematically evaluate its performance, we consider four benchmark problems with progressively increasing geometric complexity: (i) the two-dimensional Allen-Cahn equation with a moving interior hole; (ii) the two-dimensional Klein-Gordon equation with moving internal boundaries and topological changes; (iii) a nonlinear reaction-diffusion-convection system defined on a time-dependent domain undergoing large deformations; and (iv) a nonlinear diffusion equation and a Lotka-Volterra reaction-diffusion system, defined on separate complex space-time domains, thereby providing complementary benchmarks.

We first consider the Allen-Cahn equation defined on the three-dimensional space-time domain $([0, 1]^2 \setminus \mathcal{H}(t)) \times (0, 1]$:

$$\begin{cases} \frac{\partial u}{\partial t} - \Delta u + u^3 - u = f(x, y, t), & (x, y, t) \in ([0, 1]^2 \setminus \mathcal{H}(t)) \times (0, 1], \\ u(x, y, 0) = u_0(x, y), & (x, y) \in [0, 1]^2 \setminus \mathcal{H}(0), \\ u(x, y, t) = g(x, y, t), & (x, y, t) \in \partial [0, 1]^2 \cup \partial \mathcal{H}(t), \ t \in [0, 1], \end{cases}$$
(6.6)

where $\Delta u = u_{xx} + u_{yy}$ and $\mathcal{H}(t) = \{(x,y): (x-c_x(t))^2 + (y-c_y(t))^2 \le r^2\}$ denotes a circular hole of radius r=0.1 with center $c_x(t)=0.5+0.2\cos(\pi t)$, $c_y(t)=0.5+0.2\sin(\pi t)$. The source term f is chosen so that the exact solution is

$$u(x, y, t) = 2\sin(x(1-x))\sin(y(1-y))e^{t+1}.$$

Table 8 reports the numerical results of the AMIPN method for this moving-hole problem. As the numbers of collocation points $\sqrt[3]{Q}$ per subdomain and random basis functions J increase, the L^2 error of u decreases from $O(10^{-5})$ to $O(10^{-10})$, while the errors of its derivatives (u_x, u_y, u_t) decrease from $O(10^{-3} - 10^{-4})$ to $O(10^{-8} - 10^{-10})$, exhibiting a nearly exponential convergence trend. The number of outer iterations remains fixed at three, with one Jacobian evaluation per iteration, demonstrating the efficiency and stability of the method. The computational time increases predictably with J, from about 23 s to 1066 s. Figure 2 visualizes the absolute errors at t = 0, 0.20, 0.40, 0.60, 0.80, and 1.00, clearly illustrating both the temporal evolution of the circular hole and the accuracy of the method.

We next consider the two-dimensional Klein-Gordon equation posed on a square spatial domain containing two dynamically evolving internal obstacles:

$$\begin{cases} u_{tt} - \Delta u + u + \beta u^2 = f(x, y, t), & (x, y, t) \in \left([-1, 1]^2 \setminus (\Omega_1(t) \cup \Omega_2(t)) \right) \times (0, 2], \\ u(x, y, 0) = \phi(x, y), & u_t(x, y, 0) = \psi(x, y), & (x, y) \in [-1, 1]^2 \setminus (\Omega_1(0) \cup \Omega_2(0)), \\ u(x, y, t) = h(x, y, t), & (x, y, t) \in \partial([-1, 1]^2) \cup \partial\Omega_1(t) \cup \partial\Omega_2(t), \ t \in [0, 2], \end{cases}$$
(6.7)

where $\Delta u = u_{xx} + u_{yy}$, and β is a prescribed nonlinear coefficient. Each internal obstacle is defined by a level set $\Omega_i(t) = \{(x,y) \mid F_i(x,y,t) < 0\}$ (i=1,2). During the simulation, the two obstacles move toward each other, merge into a single connected component, and later separate again, thereby inducing a topological change in the computational

Table 9
The results of the AMIPN method for the Klein-Gordon equation (6.7)

(N_x, N_y, N_z)	$\sqrt[3]{Q}$	J	Solver	IT	NJ	CPU	u error	u_x error	u_y error	u_t error
		400	AMIPN	4	3	123.12	2.93e - 05	3.52e - 04	3.84e - 04	9.25e – 04
		800	AMIPN	4	3	330.70	8.93e - 07	1.34e - 05	1.47e - 05	3.67e - 05
(2, 2, 2)	30	1200	AMIPN	4	3	582.42	6.67e - 08	1.27e - 06	1.28e - 06	3.38e - 06
		1600	AMIPN	4	3	890.34	7.56e – 09	1.41e - 07	1.71 <i>e</i> – 07	4.28e - 07
		2000	AMIPN	4	3	1496.10	1.02e - 09	2.18e - 08	2.36e - 08	6.17e - 08
		2400	AMIPN	4	3	2100.97	2.12e - 10	4.90e – 09	5.40e - 09	1.42e - 08

domain. The level-set functions are

$$F_{1}(x, y, t) = x^{2} + (y - 0.5 + 0.4t)^{2} - (0.3 + 0.1\cos(4\theta_{1}))^{2},$$

$$F_{2}(x, y, t) = x^{2} + (y + 0.5 - 0.4t)^{2} - (0.3 + 0.1\cos(4\theta_{2}))^{2},$$

$$\theta_{1} = \arctan\left(\frac{y - 0.5 + 0.4t}{x}\right), \qquad \theta_{2} = \arctan\left(\frac{y + 0.5 - 0.4t}{x}\right).$$
(6.8)

Figure 3 visualizes the merging process at t = 0, 0.40, 0.80, 1.20, 1.60, and 2.00. For verification, the source term f, initial data ϕ , ψ , and boundary data h are chosen consistently. The exact solution is given by

$$u(x, y, t) = \frac{x + y + t + 2}{1 + x^2 + y^2}.$$
(6.9)

Table 9 summarizes the numerical results of the AMIPN method. With the subdomain partition fixed at $(N_x, N_y, N_z) = (2, 2, 2)$ and collocation density $\sqrt[3]{Q} = 30$, increasing the number of random features J from 400 to 2400 leads to substantial accuracy improvement. The relative error of u decreases from 2.93×10^{-5} to 2.12×10^{-10} , while the errors in u_x and u_y decrease from $O(10^{-4})$ to $O(10^{-9})$, and the u_t error decreases from $O(10^{-3} - 10^{-4})$ to $O(10^{-8})$, exhibiting spectral-like convergence. The number of outer iterations remains fixed at four, with three Jacobian evaluations per iteration, while the computational time increases from about 123 s to 2101 s as J increases. Figure 4 visualizes the absolute errors of the AMIPN method at different time instances, highlighting its robustness for problems with evolving internal obstacles and topological changes, and underscoring its capability to handle complex space-time domains with dynamic topology.

We next consider a nonlinear reaction-diffusion-convection system defined on a time-dependent perforated domain with a deforming interior hole. The governing equations are given by

$$\begin{cases} u_{t} + \mathbf{w}(x, y, t) \cdot \nabla u - \Delta u + \alpha uv = f_{1}(x, y, t), & (x, y, t) \in \left((0, 1)^{2} \setminus \Omega(t)\right) \times (0, 1], \\ v_{t} + \mathbf{w}(x, y, t) \cdot \nabla v - \Delta v + \beta e^{u}v^{2} = f_{2}(x, y, t), & (x, y, t) \in \left((0, 1)^{2} \setminus \Omega(t)\right) \times (0, 1], \\ u(x, y, 0) = \phi(x, y), & v(x, y, 0) = \psi(x, y), & (x, y) \in (0, 1)^{2} \setminus \Omega(0), \\ u(x, y, t) = h_{1}(x, y, t), & v(x, y, t) = h_{2}(x, y, t), & (x, y, t) \in \partial(0, 1)^{2} \cup \partial\Omega(t), \ t \in [0, 1]. \end{cases}$$

$$(6.10)$$

Here $\Delta = \partial_{xx} + \partial_{yy}$ and we set $\alpha = \beta = 1$. The prescribed advection velocity field is

$$\mathbf{w}(x, y, t) = \cos\left(\frac{\pi t}{10}\right) \left(\sin^2(\pi x)\sin(2\pi y), -\sin^2(\pi y)\sin(2\pi x)\right)^{\mathsf{T}}.$$

Table 10
Results of the AMIPN method for the reaction-diffusion-convection system (6.10)

(N_x, N_y, N_z)	$\sqrt[3]{Q}$	J	Solver	IT	NJ	CPU	u error	v error
	20	400 800	AMIPN AMIPN	3	2 2	141.81 422.22	6.99e - 05 1.53e - 06	
(2, 2, 2)	25	1200 1600	AMIPN AMIPN	3	2 2	1294.65 2817.73	6.04e - 08 3.88e - 09	3.91e - 08 3.99e - 09
	30	1600 2000	AMIPN AMIPN	3	2 2	4244.36 5438.12	5.03e - 09 4.76e - 10	$3.25e - 09 \\ 5.48e - 10$

The computational domain is the unit square $(0, 1)^2$ with a time-dependent interior hole $\Omega(t)$. It is initially defined as

$$\Omega(0) = \left\{ (x, y) \in (0, 1)^2 \mid (x - 0.5)^2 + (y - 0.75)^2 \le 0.15^2 \right\}.$$

The interior perforation $\Omega(t)$ evolves over time according to the prescribed advection velocity field $\mathbf{w}(x, y, t)$. To track the motion of the perforation boundary, the boundary points $\mathbf{X}(t) \in \partial \Omega(t)$ are advected by the flow field according to

$$\frac{d\mathbf{X}}{dt} = \mathbf{w}(\mathbf{X}(t), t), \qquad \mathbf{X}(0) \in \partial\Omega(0).$$

The trajectories of boundary points are numerically integrated using a fifth-order Runge-Kutta scheme. At each selected time t, the updated positions of the advected boundary points are used to reconstruct the moving interface $\partial\Omega(t)$, thereby defining the time-dependent perforated computational domain $(0,1)^2 \setminus \Omega(t)$. For verification, the source terms f_1, f_2 and the boundary/initial data are chosen consistently with the exact solution

$$u(x, y, t) = \sin(x(1-x))\sin(y(1-y))e^t,$$
 $v(x, y, t) = \sin(\pi x)\sin(\pi y)\sin(\pi t).$

Table 10 reports the numerical results of the AMIPN method for the nonlinear reaction-diffusion-convection system on a time-dependent domain with a deforming interior hole. The relative L^2 errors of u and v decrease from $O(10^{-5}-10^{-6})$ to $O(10^{-10})$, exhibiting spectral-like convergence and confirming the spectral accuracy of the proposed method for this challenging large-deformation problem. Moreover, even in large-scale and potentially ill-conditioned settings, the number of outer iterations remains fixed at three, with only two Jacobian evaluations per iteration, demonstrating the efficiency and robustness of the proposed approach.

Table 11 reports the preconditioning time per outer iteration and the number of LSQR iterations in the inner loop. The results indicate that the preconditioning stage constitutes the dominant portion of the computational cost. By reusing the preconditioned Jacobian across multiple inner iterations, the AMIPN method substantially reduces the number of preconditionings, thereby reducing the overall cost compared with IPN. Figure 5 illustrates the absolute errors of u and v at t = 0, 0.35, 0.70, 1.00. The white region denotes the interior hole $\Omega(t)$, which deforms from an initial circular shape into a highly elongated snake-like geometry under the prescribed advection field, clearly demonstrating the capability of AMIPN to maintain high accuracy and stability in strongly deforming domains with time-dependent geometries.

We next consider a Lotka-Volterra reaction-diffusion system defined on a perforated space-time domain:

$$\begin{cases} u_{t} - \Delta u - u + uv = f_{1}(x, y, t), & (x, y, t) \in \mathcal{D}^{*}, \\ v_{t} - \Delta v + v - uv = f_{2}(x, y, t), & (x, y, t) \in \mathcal{D}^{*}, \\ u(x, y, 0) = u_{0}(x, y), & v(x, y, 0) = v_{0}(x, y), & (x, y) \in \Omega, \\ u(x, y, t) = g_{1}(x, y, t), & v(x, y, t) = g_{2}(x, y, t), & (x, y, t) \in \partial\Omega \times (0, 2], \end{cases}$$

$$(6.11)$$

Table 11
Preconditioning time per outer iteration and the number of LSQR steps in the inner iteration

(N_x, N_y, N_z)	$\sqrt[3]{Q}$	J	Outer Iter	PCPU(s)	lter 1	Iter 2	Iter 3	TLI
			1	476.95	33	31	34	98
		1200	2	478.64	32	11		43
(2, 2, 2)	2, 2, 2) 25		3		9			9
(2,2,2)	25		1	1072.94	35	34	35	104
		1600	2	1052.04	39	16		55
			3		14			14

Table 12
Results of the AMIPN method for Lotka-Volterra reaction-diffusion system (6.11)

(N_x, N_y, N_z)	$\sqrt[3]{Q}$	J	Solver	IT	NJ	u error	v error
	20	400 800	AMIPN AMIPN	3	2 2		3.70 <i>e</i> – 05 8.46 <i>e</i> – 07
(2, 2, 2)	25	1200 1600	AMIPN AMIPN	3	2 2		5.69e - 08 8.07e - 09
	30	1600 2000	AMIPN AMIPN	3	2 2		7.12 <i>e</i> – 09 1.64 <i>e</i> – 09

where $\Delta u = u_{xx} + u_{yy}$ and $\Delta v = v_{xx} + v_{yy}$. The source terms f_1, f_2 , together with the boundary and initial data, are derived from the manufactured exact solution

$$u(x, y, t) = \sin(\pi x)\sin(\pi y)e^{t}, \quad v(x, y, t) = \frac{x^{2} + y^{2} + t^{2} + 2}{t + 1}.$$

The spatial background domain is the square $\Omega_{sq} = [-1, 1]^2$, from which a star-shaped region

$$S = \left\{ (x, y) : \left(x - c_x \right)^2 + \left(y - c_y \right)^2 \le r(\theta)^2, \quad r(\theta) = 0.4 + 0.2 \sin(20\theta) \right\},$$

centered at $(c_x, c_y) = (0.02\sqrt{5}, 0.02\sqrt{5})$, is excised. The resulting computational domain is $\Omega = \Omega_{\rm sq} \setminus \mathcal{S}$. Extending in time, the full space-time domain is defined as

$$\mathcal{D}^* = \Omega \times (0, 2] = ([-1, 1]^2 \times (0, 2]) \setminus (\mathcal{S} \times (0, 2]),$$

which can be interpreted as a three-dimensional column $[-1,1]^2 \times (0,2]$ with a star-shaped cylindrical void removed along the time axis. This construction results in a highly complex perforated space-time geometry, with oscillatory internal boundaries and nontrivial embeddings, thereby posing substantial challenges for generating high-quality meshes.

The results in Table 12 demonstrate that the proposed AMIPN method achieves both high accuracy and stable convergence for the Lotka-Volterra reaction-diffusion system. As the number of random basis functions J increases, the errors in u and v decrease significantly, from the order of $10^{-4} - 10^{-5}$ down to $10^{-8} - 10^{-9}$. Throughout all tests, the number of outer iterations and Jacobian evaluations remain nearly constant (about 3 and 2, respectively), indicating that the computational cost does not grow with problem size. Figure 6 presents the cross-sectional errors of u and v at t = 0, 0.7, 1.40, and 2.00.

Table 13
The results of the AMIPN method for the nonlinear diffusion problem (6.12)

(N_x, N_y, N_z)	$\sqrt[3]{Q}$	J	Solver	IT	NJ	u error	u_x error	u_y error	u_t error
(2,2,2)	20	400 800				2.01e - 05 6.67e - 07			
	25	1200 1600				7.43e - 08 9.84e - 09			
	30	2000 2400	AMIPN AMIPN	5 5		$2.68e - 09 \\ 6.00e - 10$			

We finally consider a nonlinear diffusion problem defined on a complex space-time domain:

$$\begin{cases} \frac{\partial u}{\partial t} - \nabla \cdot \left((1 + u^2) \nabla u \right) = f(x, y, t), & (x, y, t) \in \mathcal{D}^*, \\ u(x, y, 0) = u_0(x, y), & (x, y) \in \Omega, \\ u(x, y, t) = g(x, y, t), & (x, y, t) \in \partial \Omega \times (0, 1], \end{cases}$$

$$(6.12)$$

where $\Delta u = u_{xx} + u_{yy}$ and $a(u) = 1 + u^2$ is the nonlinear diffusion coefficient. The source term f and the boundary/initial data g, u_0 are derived from the manufactured exact solution

$$u(x, y, t) = \frac{2(x + y + t)}{1 + x^2 + y^2} \left[\tanh\left(\sin(\pi x)\cos(\pi y)e^{-t}\right) + 1 \right].$$

The spatial domain Ω is constructed from the background square $\Omega_{\text{sq}} = (1.5, 2.5) \times (1.0, 2.0)$ by removing three circular holes $C^- = \{B(\mathbf{c}_k, r_k)\}_{k=1}^3$ and embedding four circular inclusions $C^+ = \{B(\tilde{\mathbf{c}}_j, \tilde{r}_j)\}_{j=1}^4$. The resulting computational domain is

$$\Omega = \left(\Omega_{\mathrm{sq}} \setminus \bigcup_{k=1}^3 B(\mathbf{c}_k, r_k)\right) \cup \bigcup_{j=1}^4 B(\tilde{\mathbf{c}}_j, \tilde{r}_j).$$

The full space-time domain $\mathcal{D}^* = \Omega \times (0,1]$ may thus be interpreted as a three-dimensional column $\Omega_{sq} \times (0,1]$ with multiple cylindrical voids removed and inclusions embedded, producing a perforated structure of considerable geometric complexity. Notably, two removed disks nearly touch at the point (1.935, 1.78) (see Figure 7), which is reported to cause mesh generation failures in commercial FEM software such as COMSOL.

Table 13 presents the numerical results of the AMIPN method for (6.12) on this geometrically intricate domain. As the collocation density $\sqrt[3]{Q}$ and the number of random features J increase, the accuracy improves significantly. The relative L^2 error of u decreases from 2.01×10^{-5} (at $\sqrt[3]{Q} = 20$, J = 400) to 6.00×10^{-10} (at $\sqrt[3]{Q} = 30$, J = 2400), while the errors of its first derivatives (u_x , u_y , u_t) decrease from $O(10^{-3}-10^{-4})$ to $O(10^{-7}-10^{-8})$. Figure 8 shows that the cross-sectional error at the final time t = 1.0 reaches the order of 10^{-10} , confirming the capability of the proposed method to deliver high accuracy on geometrically intricate space-time domains where traditional mesh-based methods may fail.

In summary, the four benchmark problems with moving holes, topological changes, large deformations, and complex space-time geometries demonstrate that the AMIPN method consistently delivers robustness, scalability, and spectral-like accuracy. With only a few outer iterations and Jacobian evaluations, errors are reduced to $O(10^{-9}-10^{-11})$, underscoring its strong potential for solving challenging time-dependent PDEs on domains where conventional meshbased methods often break down.

7. Conclusions

In this work, we developed two nonlinear solvers designed for large-scale and ill-conditioned nonlinear least-squares problems arising from RFM discretizations of nonlinear PDEs. The inexact Newton method with right

Table 14
The results of the AMIPN method for 3D nonlinear elliptic equation (A.1)

(N_x, N_y, N_z)	$\sqrt[3]{Q}$	J	Solver	IT	NJ	CPU	u error	u_x error	u_y error	u_z error
		400	AMIPN	2	1	114.80	2.37e - 03	1.58e - 02	1.57e - 02	1.61 <i>e</i> – 02
		800	AMIPN	2	1	247.13	6.60e – 04	6.32e - 03	6.25e - 03	6.31e - 03
(2, 2, 2)	40	1200	AMIPN	2	1	405.85	3.09e - 04	3.40e - 03	3.36e - 03	3.39e - 03
		1600	AMIPN	2	1	803.16	1.60e – 04	1.88e - 03	1.86e - 03	1.87e - 03
		2000	AMIPN	3	1	1346.66	7.38e - 05	8.70e - 04	9.30e – 04	8.79e - 04
		2400	AMIPN	3	1	1625.84		refe	rence	

preconditioning integrates randomized preconditioning with Krylov iterations and derivative-free line searches, thereby improving robustness and stability. Its adaptive multi-step extension further reduces redundant computations by reusing preconditioned Jacobians with an adaptive early-stopping strategy, resulting in enhanced efficiency without loss of accuracy.

Extensive numerical experiments on three-dimensional steady-state PDEs-including elliptic, diffusion-reaction, Helmholtz, and Gray-Scott equations-as well as two-dimensional timedependent problems on domains with moving holes, topological changes, large deformations, and complex geometries confirm the effectiveness of the proposed solvers. The results consistently show spectral-like convergence, with relative errors reduced to the order of $10^{-9} - 10^{-11}$ within only a few outer iterations and a small number of Jacobian evaluations. Compared with conventional FEM and FDM, the proposed methods achieve improvements of four to seven orders of magnitude under the same collocation density, while also outperforming recent machine-learning-based approaches such as PINNs and WANs. Future work will focus on a rigorous convergence analysis of IPN and AMIPN and on extending the framework to more challenging classes of nonlinear PDEs, further strengthening its applicability and reliability in large-scale scientific and engineering computations.

A. Supplementary numerical examples

This appendix presents several additional numerical examples beyond the main test cases reported in the paper. We first consider a three-dimensional steady-state nonlinear elliptic problem defined on the unit cube $(0, 1)^3$:

$$\begin{cases} -\nabla \cdot (\Lambda(u)\nabla u) = 1, & (x, y, z) \in (0, 1)^3, \\ u = 0, & (x, y, z) \in \partial(0, 1)^3, \end{cases}$$
(A.1)

where the nonlinear diffusion coefficient is given by $\Lambda(u) = 1 + u^2$. Since no closed-form exact solution is available, this problem is used to examine the numerical self-convergence of the proposed method.

As shown in Table 14, the proposed AMIPN method exhibits a clear trend of numerical convergence for this 3D nonlinear elliptic problem. The solution obtained with the largest parameter setting (J = 2400) is taken as the reference solution, and the resulting errors for other cases decrease steadily as J increases. In particular, when J = 2000, the error of u reaches the order of 10^{-5} (7.38×10^{-5}), while the errors of its first derivatives (u_x, u_y, u_z) are on the order of 10^{-4} ($8.70 \times 10^{-4} \sim 9.30 \times 10^{-4}$).

Table 15
The results of the AMIPN method for the KdV equation (A.2)

(N_x, N_y, N_t)	$\sqrt[3]{Q}$	J	Solver	ΙΤ	NJ	CPU	u error	u_x error	u_y error	u_t error
	20	400 800	AMIPN AMIPN	4 4	3	50.21 139.99	5.48 <i>e</i> – 06 6.74 <i>e</i> – 08	3.68 <i>e</i> – 04 6.05 <i>e</i> – 06	3.79 <i>e</i> – 04 5.83 <i>e</i> – 06	1.82e - 03 $3.63e - 05$
(2, 2, 2)	25	1200 1600	AMIPN AMIPN	4 4	3	423.17 668.82	3.10 <i>e</i> – 09 3.35 <i>e</i> – 10	3.28e - 07 $3.05e - 08$	3.26 <i>e</i> – 07 3.03 <i>e</i> – 08	$2.22e - 06 \\ 3.06e - 07$
	30	1600 2000 2400	AMIPN AMIPN AMIPN	5 5 5	3 3 3	918.26 1381.28 1906.82	4.30 <i>e</i> – 10 1.21 <i>e</i> – 10 1.22 <i>e</i> – 11	3.85e - 08 5.78e - 09 8.68e - 10	3.78e - 08 5.66e - 09 9.22e - 10	3.86e - 07 $1.15e - 07$ $1.46e - 08$

We next consider the two-dimensional Korteweg-de Vries (KdV) initial-boundary value problem defined on the space-time domain $(x, y, t) \in \Omega = [0, 1]^2 \times [0, 1]$:

$$\begin{cases} u_t - u \, u_x - u \, u_y + u_{xxx} + u_{yyy} = f(x, y, t), & (x, y, t) \in (0, 1)^2 \times (0, 1], \\ u(0, y, t) = g_1(y, t), & u(1, y, t) = g_2(y, t), & u_x(0, y, t) = g_3(y, t), & y \in [0, 1], \ t \in [0, 1], \\ u(x, 0, t) = p_1(x, t), & u(x, 1, t) = p_2(x, t), & u_y(x, 0, t) = p_3(x, t), & x \in [0, 1], \ t \in [0, 1], \\ u(x, y, 0) = h(x, y), & (x, y) \in [0, 1]^2. \end{cases}$$
(A.2)

The source term f and the boundary-initial data (g_i, p_i, h) are constructed from the manufactured exact solution

$$u(x, y, t) = 10 - (x^3 + y^3 + t^3)$$
(A.3)

As shown in Table 15, the AMIPN method exhibits a clear trend of numerical convergence for the KdV equation. As the collocation density $\sqrt[3]{Q}$ and the number of random features J increase, the relative L^2 -error of u decreases from 5.48×10^{-6} to 1.22×10^{-11} , while the errors of its derivatives (u_x, u_y, u_t) are simultaneously reduced from the order of $10^{-4} \sim 10^{-3}$ to the order of $10^{-9} \sim 10^{-8}$. Throughout all tested cases, convergence is achieved within only 4-5 outer iterations, each requiring merely 3 Jacobian evaluations, demonstrating the high efficiency and robustness of the proposed method even for this challenging nonlinear problem.

We then consider the two-dimensional nonlinear Schrödinger equation with Dirichlet boundary conditions:

$$\begin{cases} i \frac{\partial h}{\partial t} + \frac{1}{2} \left(\frac{\partial^2 h}{\partial x^2} + \frac{\partial^2 h}{\partial y^2} \right) + |h|^2 h = f(x, y, t), & (x, y, t) \in (0, 1)^2 \times (0, 1], \\ h(a, y, t) = g_1(y, t), & h(b, y, t) = g_2(y, t), & y \in [0, 1], \ t \in [0, 1], \\ h(x, c, t) = g_3(x, t), & h(x, d, t) = g_4(x, t), & x \in [0, 1], \ t \in [0, 1], \\ h(x, y, 0) = g_0(x, y), & (x, y) \in [0, 1]^2. \end{cases}$$
(A.4)

The exact solution is given by h = u + iv,

$$u = (x-1)^3 + (y-1)^3 + (t-1)^3$$
, $v = 2\sin(x(1-x))\sin(y(1-y))e^t$

The results in Table 16 indicate that the AMIPN method maintains consistently high accuracy across all tested configurations. Even at moderate settings ($\sqrt[3]{Q} = 20$, J = 800), the errors are already reduced to 8.79×10^{-7} for u, 6.67×10^{-6} for v, and 1.22×10^{-6} for h. Further increasing $\sqrt[3]{Q}$ and J yields steadily improved accuracy, ultimately reaching 3.04×10^{-10} , 2.05×10^{-9} , and 4.01×10^{-10} for u, v, and h, respectively.

Table 16
The results of the AMIPN method for the Schrödinger equation (A.4)

(N_x, N_y, N_t)	$\sqrt[3]{Q}$	J	Solver	IT	NJ	u error	v error	h error
	20	400 800	AMIPN AMIPN	4 4	3	2.75e - 05 8.79e - 07	1.86e – 04 6.67e – 06	3.62e - 05 1.22e - 06
(2, 2, 2)	25	1200 1600	AMIPN AMIPN	4 4	3	1.95e - 08 $3.18e - 09$	$1.47e - 07 \\ 2.37e - 08$	2.70e - 08 4.38e - 09
	30	1600 2000 2400	AMIPN AMIPN AMIPN	5 4 4	3 3 3	1.74 <i>e</i> - 09 3.35 <i>e</i> - 10 3.04 <i>e</i> - 10	1.32e - 08 $2.34e - 09$ $2.05e - 09$	2.42e - 09 $4.48e - 10$ $4.01e - 10$

Table 17
The results of the AMIPN method for the Burgers equations (A.5)

(N_x, N_y, N_t)	$\sqrt[3]{Q}$	J	Method	ΙΤ	NJ	u error	v error
	20	400 800	AMIPN AMIPN	4 4	3	4.93 <i>e</i> - 04 5.11 <i>e</i> - 05	$4.15e - 04 \\ 3.20e - 05$
(2, 2, 2)	25	1200 1600	AMIPN AMIPN	4 4	3	1.15 <i>e</i> – 05 3.50 <i>e</i> – 06	7.56e - 06 2.23e - 06
	30	1600 2000 2400	AMIPN AMIPN AMIPN	4 4 4	3 3 3	3.87e - 06 1.17e - 06 6.23e - 07	2.80e - 06 $7.20e - 07$ $3.78e - 07$

We further solve the following two-dimensional coupled unsteady Burgers equations using the proposed method:

$$\begin{split} \partial_t u + u \partial_x u + v \partial_y u &= \frac{1}{\text{Re}} \left(\partial_x^2 u + \partial_y^2 u \right), \\ \partial_t v + u \partial_x v + v \partial_y v &= \frac{1}{\text{Re}} \left(\partial_x^2 v + \partial_y^2 v \right), \end{split} \quad x, y \in [0, 1], \ t \in [0, 1]. \end{split} \tag{A.5}$$

Here, u and v denote the velocity components along the x - and y-directions, respectively. The Reynolds number Re is defined as Re = UL/v, where U and L are the characteristic velocity and length, and v is the kinematic viscosity of the fluid. The exact solution can be obtained [44] as

$$u(x, y, t) = \frac{3}{4} - \frac{1}{4[1 + \exp((-4x + 4y - t) \operatorname{Re}/32)]}$$
$$v(x, y, t) = \frac{3}{4} + \frac{1}{4[1 + \exp((-4x + 4y - t) \operatorname{Re}/32)]}$$

subject to Dirichlet boundary conditions on all boundaries. In this study, the Reynolds number is set to Re = 100.

Table 17 presents the numerical results for the Burgers equations. As shown in Figure 9, the absolute error distributions of u (left) and v (right) at the final time t = 1.00 indicate that the relatively larger errors are localized near the left boundary, while the errors remain small in the interior region and along the other boundaries.

We finally consider the two-dimensional incompressible Navier-Stokes equations to further verify the accuracy of the proposed method. Let the velocity field be $\mathbf{u} = (u(x, y, t), v(x, y, t))$ and the pressure field be p(x, y, t). The

Table 18The results of the AMIPN method for the Navier-Stokes equations (A.6).

(N_x, N_y, N_t)	$\sqrt[3]{Q}$	J	(m, n)	Method	IT	NJ	u error	v error	p error
	20	400	(235200, 9600)	AMIPN	4	3	1.63e - 03	1.55e - 03	1.63e - 02
		800	(235200, 19200)	AMIPN	4	3	5.96e – 05	6.11 <i>e</i> – 05	8.76e - 04
(2, 2, 2)	25	1200	(442500, 28800)	AMIPN	4	3	4.47e - 06	4.63e - 06	1.32e - 04
		1600	(442500, 38400)	AMIPN	4	3	5.43e - 07	2.04e - 04	3.51e - 03
	30	1600	(745200, 38400)	AMIPN	4	3	5.94e - 07	6.16e - 07	1.44e - 05
	2.0	2000	(745200, 48000)	AMIPN	4	3	9.47e - 08	9.01e - 08	5.65e - 06

governing system is given by

$$\begin{cases} \frac{\partial u}{\partial t} + u \frac{\partial u}{\partial x} + v \frac{\partial u}{\partial y} = -\frac{\partial p}{\partial x} + \left(\frac{\partial^2 u}{\partial x^2} + \frac{\partial^2 u}{\partial y^2}\right), \\ \frac{\partial v}{\partial t} + u \frac{\partial v}{\partial x} + v \frac{\partial v}{\partial y} = -\frac{\partial p}{\partial y} + \left(\frac{\partial^2 v}{\partial x^2} + \frac{\partial^2 v}{\partial y^2}\right), \\ \frac{\partial u}{\partial x} + \frac{\partial v}{\partial y} = 0, \end{cases}$$

$$(A.6)$$

Following [45], the exact solution is prescribed as

$$u(x, y, t) = -\cos(\pi x)\sin(\pi y)e^{-2\pi^2 t},$$

$$v(x, y, t) = \sin(\pi x)\cos(\pi y)e^{-2\pi^2 t},$$

$$p(x, y, t) = -\frac{\cos(2\pi x) + \cos(2\pi y)}{4}e^{-4\pi^2 t},$$

and Dirichlet boundary conditions are imposed on all boundaries.

Table 18 summarizes the numerical results obtained by the AMIPN method, including the number of outer iterations, the number of Jacobian evaluations, and the L^2 -relative errors of u, v, and p. As shown in the table, the problem size (i.e., the numbers of equations m and unknowns n) grows rapidly with the increase of the collocation density $\sqrt[3]{Q}$ and the number of random basis functions J, reaching up to (745,200, 48,000) in the largest case. Even for such extremely large-scale NLS systems, the AMIPN method achieves rapid convergence within only 4 outer iterations and 3 Jacobian evaluations, while the relative errors decrease steadily—from $10^{-3} \sim 10^{-2}$ at J = 400 to $10^{-8} \sim 10^{-6}$ at J = 2000—demonstrating both the scalability and the accuracy of the proposed approach for the incompressible Navier-Stokes problems.

Acknowledgements

This work is partially supported by the National Key R&D Program of China (No. 2022YFA1005200, No. 2022YFA1005202, and No.2022YFA1005203), the NSFC Major Research Plan - Interpretable and General Purpose Next-generation Artificial Intelligence (Nos. 92270001 and 92370205), NSFC grant 12425113, and Key Laboratory of the Ministry of Education for Mathematical Foundations and Applications of Digital Technology, University of Science and Technology of China.

CRediT authorship contribution statement

Longze Tan: Writing-review & editing, Writing-original draft, Visualization, Validation, Software, Methodology, Investigation, Data curation, Mathematical analysis, Formal analysis, Conceptualization. Xiaohe Yue: Validation, Software, Visualization, Data curation. Jingrun Chen: Writing-review & editing, Writing-original draft, Visualization, Validation, Supervision, Project administration, Methodology, Investigation, Funding acquisition, Formal analysis,

Conceptualization. Jiamin Jiang: Writing-review & editing, Writing-original draft, Data curation, Methodology, Formal analysis.

Declaration of competing interest

The authors confirm that they have no financial or personal conflicts of interest that could have influenced the findings presented in this paper.

Data availability

No data was used for the research described in the article.

References

- [1] R. J. LeVeque, Finite difference methods for ordinary and partial differential equations: steady-state and time-dependent problems, SIAM, 2007
- [2] O. C. Zienkiewicz, R. L. Taylor, J. Z. Zhu, The Finite Element Method: Its Basis and Fundamentals, Elsevier, 2005.
- [3] J. Shen, T. Tang, L.-L. Wang, Spectral methods: algorithms, analysis and applications, Vol. 41, Springer Science & Business Media, 2011.
- [4] A. Bueno-Orovio, V. M. Pérez-García, F. H. Fenton, Spectral methods for partial differential equations in irregular domains: the spectral smoothed boundary method, SIAM J. Sci. Comput. 28 (3) (2006) 886–900.
- [5] A. Bueno-Orovio, V. M. Pérez-García, Spectral smoothed boundary methods: the role of external boundary conditions, Numer. Methods Partial. 22 (2) (2006) 435–448.
- [6] X. Li, J. Lowengrub, A. Rätz, A. Voigt, Solving pdes in complex geometries: a diffuse domain approach, Commun. Math. Sci. 7 (1) (2009) 81.
- [7] F. Yu, Z. Guo, J. Lowengrub, Higher-order accurate diffuse-domain methods for partial differential equations with dirichlet boundary conditions in complex, evolving geometries, J. Comput. Phys. 406 (2020) 109174.
- [8] L. Chen, H. Wei, M. Wen, An interface-fitted mesh generator and virtual element methods for elliptic interface problems, J. Comput. Phys. 334 (2017) 327–348.
- [9] M. Raissi, P. Perdikaris, G. E. Karniadakis, Physics-informed neural networks: A deep learning framework for solving forward and inverse problems involving nonlinear partial differential equations, J. Comput. Phys. 378 (2019) 686–707.
- [10] J. Sirignano, K. Spiliopoulos, Dgm: A deep learning algorithm for solving partial differential equations, J. Comput. Phys. 375 (2018) 1339– 1364.
- [11] Y. Zang, G. Bao, X. Ye, H. Zhou, Weak adversarial networks for high-dimensional partial differential equations, J. Comput. Phys. 411 (2020) 109409.
- [12] W. E, B. Yu, The deep ritz method: A deep learning-based numerical algorithm for solving variational problems, Commun. Math. Stat. 6 (1) (2018) 1–12.
- [13] Y. Liao, P. Wang, Deep nitsche method: Deep ritz method with essential boundary conditions, Commun. Comput. Phys. 29 (5) (2021) 1365–1384.
- [14] L. Lyu, Z. Zhang, M. Chen, J. Chen, MIM: A deep mixed residual method for solving high-order partial differential equations, J. Comput. Phys. 452 (2022) 110930.
- [15] E. Weinan, et al., The dawning of a new era in applied mathematics, Notices Amer. Math. Soc. 68 (4) (2021) 565-571.
- [16] G. E. Karniadakis, I. G. Kevrekidis, L. Lu, P. Perdikaris, S. Wang, L. Yang, Physics-informed machine learning, Nat. Rev. Phys. 3 (6) (2021) 422–440.
- [17] K. D. B. J. Adam, et al., A method for stochastic optimization, arXiv preprint arXiv:1412.6980 1412 (6) (2014).
- [18] D. C. Liu, J. Nocedal, On the limited memory bfgs method for large scale optimization, Math. Program. 45 (1) (1989) 503-528.
- [19] S. Wang, Y. Teng, P. Perdikaris, Understanding and mitigating gradient flow pathologies in physics-informed neural networks, SIAM J. Sci. Comput. 43 (5) (2021) A3055–A3081.
- [20] Y. Yang, M. Hou, J. Luo, A novel improved extreme learning machine algorithm in solving ordinary differential equations by legendre neural network methods, Adv. Difference Equ. 2018 (1) (2018) 469.
- [21] F. Calabrò, G. Fabiani, C. Siettos, Extreme learning machine collocation for the numerical solution of elliptic pdes with sharp gradients, Comput. Methods Appl. Mech. Engrg. 387 (2021) 114188.
- [22] S. Dong, Z. Li, Local extreme learning machines and domain decomposition for solving linear and nonlinear partial differential equations, Comput. Methods Appl. Mech. Engrg. 387 (2021) 114129.
- [23] J. Chen, X. Chi, Z. Yang, et al., Bridging traditional and machine learning-based algorithms for solving PDEs: the random feature method, J. Mach. Learn. 1 (2022) 268–98.
- [24] X. Chi, J. Chen, Z. Yang, The random feature method for solving interface problems, Comput. Methods Appl. Mech. Eng. 420 (2024) 116719.
- [25] J. Chen, W. E, Y. Luo, The random feature method for time-dependent problems, East Asian J. Appl. Math. 13 (3) (2023) 435–463.
- [26] Z. Mei, H. Xie, H. Yong, Z. Yang, J. Chen, Solving diffusion problems by a random feature method, East Asian J. Appl. Math. 1 (2024) 1–20.
- [27] K.-X. Xiong, Z. Zhang, J.-R. Chen, Y.-X. Luo, The random feature method for elliptic eigenvalue problems, Adv. Appl. Math. Mech. 17 (4) (2025) 1133–1170.
- [28] Z. Mei, Y. Huang, J. Chen, Direct mesh-free topology optimization using random feature method, Computer-Aided Design (2025) 103939.

Robust and efficient solvers

- [29] Y. Sun, J. Chen, Two-level random feature methods for elliptic partial differential equations over complex domains, Comput. Methods Appl. Mech. Eng. 441 (2025) 117961.
- [30] J. Chen, Z. Ma, K. Wu, A micro-macro decomposition-based asymptotic-preserving random feature method for multiscale radiative transfer equations, Journal of Computational Physics (2025) 114103.
- [31] C. T. Kelley, Iterative Methods for Optimization, Vol. 18 of Frontiers in Applied Mathematics, SIAM, Philadelphia, 1999.
- [32] K. Levenberg, A method for the solution of certain non-linear problems in least squares, Quart. Appl. Math. 2 (2) (1944) 164-168.
- [33] D. W. Marquardt, An algorithm for least-squares estimation of nonlinear parameters, J. Soc. Indust. Appl. Math. 11 (2) (1963) 431–441.
- [34] J. J. Moré, The levenberg-marquardt algorithm: implementation and theory, in: Numerical Analysis, Proceedings of the 7th Biennial Conference, Dundee, 1977, Vol. 630 of Lecture Notes in Mathematics, Springer, Berlin, 1978, pp. 105–116.
- [35] Y.-x. Yuan, Trust region algorithms for nonlinear equations, Hong Kong Baptist University, Department of Mathematics, 1994.
- [36] N. Yamashita, M. Fukushima, On the rate of convergence of the levenberg-marquardt method, in: Topics in numerical analysis: with special emphasis on nonlinear problems, Springer, 2001, pp. 239–249.
- [37] J. Fan, Y.-x. Yuan, On the quadratic convergence of the levenberg-marquardt method without nonsingularity assumption, Computing 74 (1) (2005) 23–39.
- [38] J. J. Moré, D. C. Sorensen, Computing a trust region step, SIAM J. Sci. Stat. Comput. 4 (3) (1983) 553-572.
- [39] M. Charikar, K. Chen, M. Farach-Colton, Finding frequent items in data streams, Theor. Comput. Sci. 312 (1) (2004) 3–15.
- [40] K. L. Clarkson, D. P. Woodruff, Low-rank approximation and regression in input sparsity time, Journal of the ACM 63 (6) (2017) 1–45.
- [41] D. P. Woodruff, Sketching as a tool for numerical linear algebra, Found. Trends Theor. Comput. Sci. 10 (1–2) (2014) 1–157.
- [42] J. Chen, L. Tan, High-precision randomized iterative methods for the random feature method, arXiv preprint arXiv:2409.15818 (2024).
- [43] M. Alnæs, J. Blechta, J. Hake, A. Johansson, B. Kehlet, A. Logg, C. Richardson, J. Ring, M. E. Rognes, G. N. Wells, The fenics project version 1.5, Arch. Numer. Software 3 (100) (2015).
- [44] A. Baeza, P. Mulet, Adaptive mesh refinement techniques for high-order shock capturing schemes for multi-dimensional hydrodynamic simulations, Int. J. Numer. Methods Fluids 52 (4) (2006) 455–471.
- [45] C. R. Ethier, D. Steinman, Exact fully 3d navier-stokes solutions for benchmarking, Int. J. Numer. Methods Fluids 19 (5) (1994) 369-375.

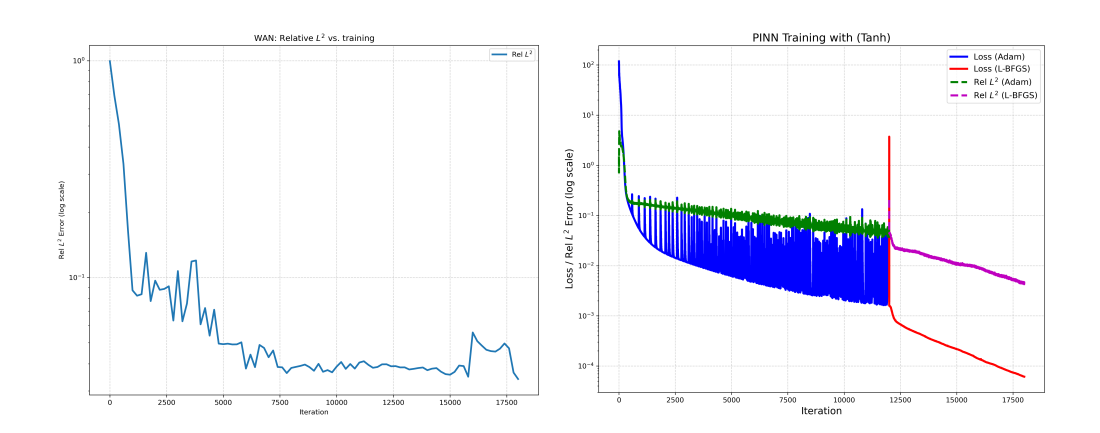


Figure 1: Left: WAN (Relative L^2 vs. training); Right: PINN (Relative L^2 and loss vs. training).

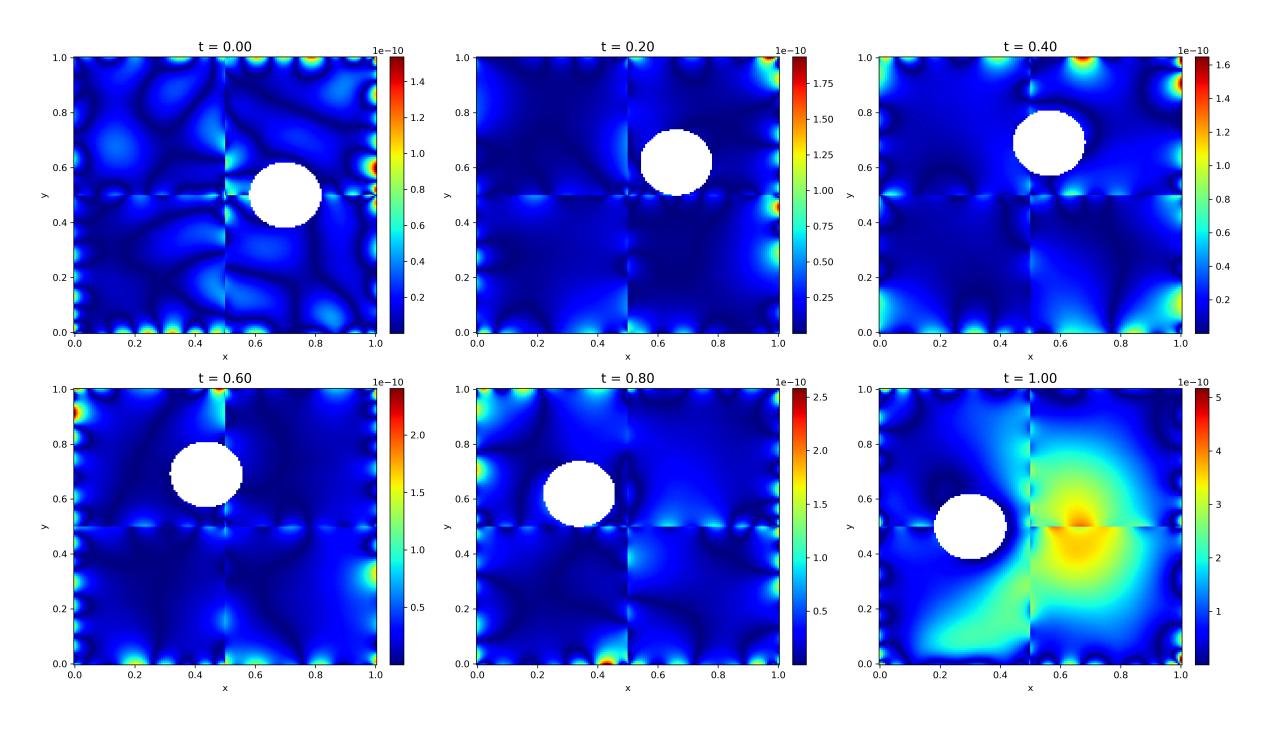


Figure 2: Absolute error on the x-y plane at times t = 0, 0.20, 0.40, 0.60, 0.80,and 1.00 for the Allen–Cahn equation (6.6)

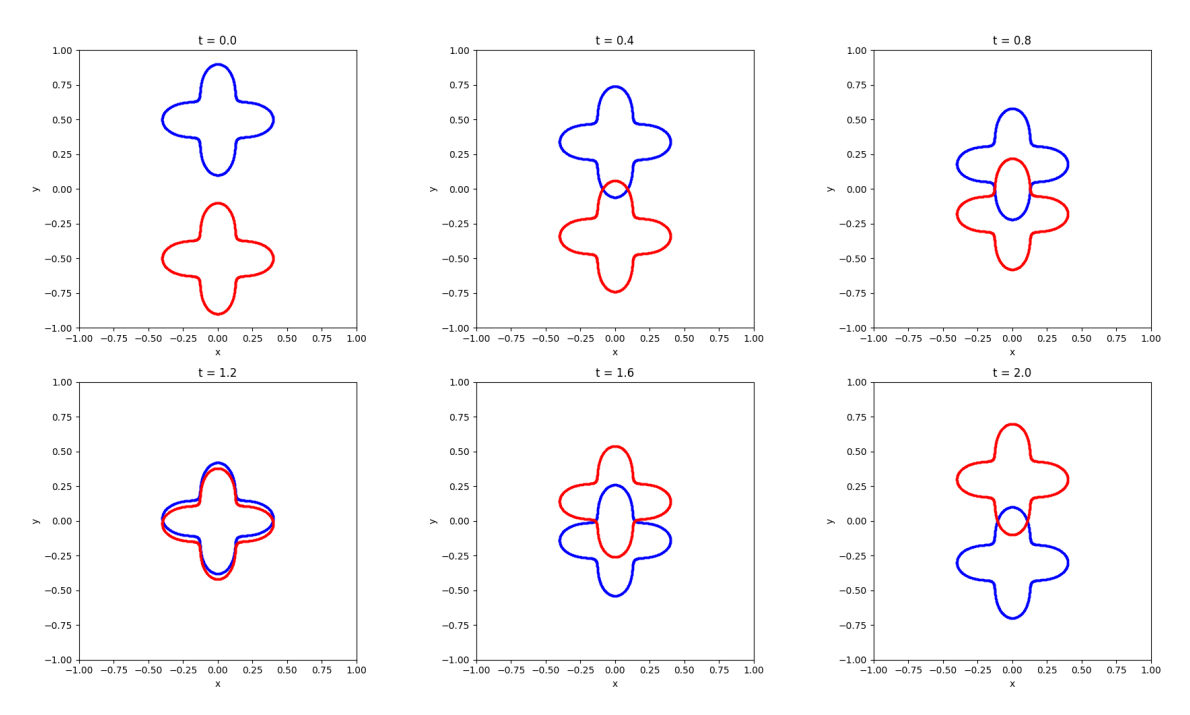


Figure 3: The evolution of the zero level sets of $F_1(x, y, t)$ and $F_2(x, y, t)$, where the corresponding excised regions first merge and then split over time.

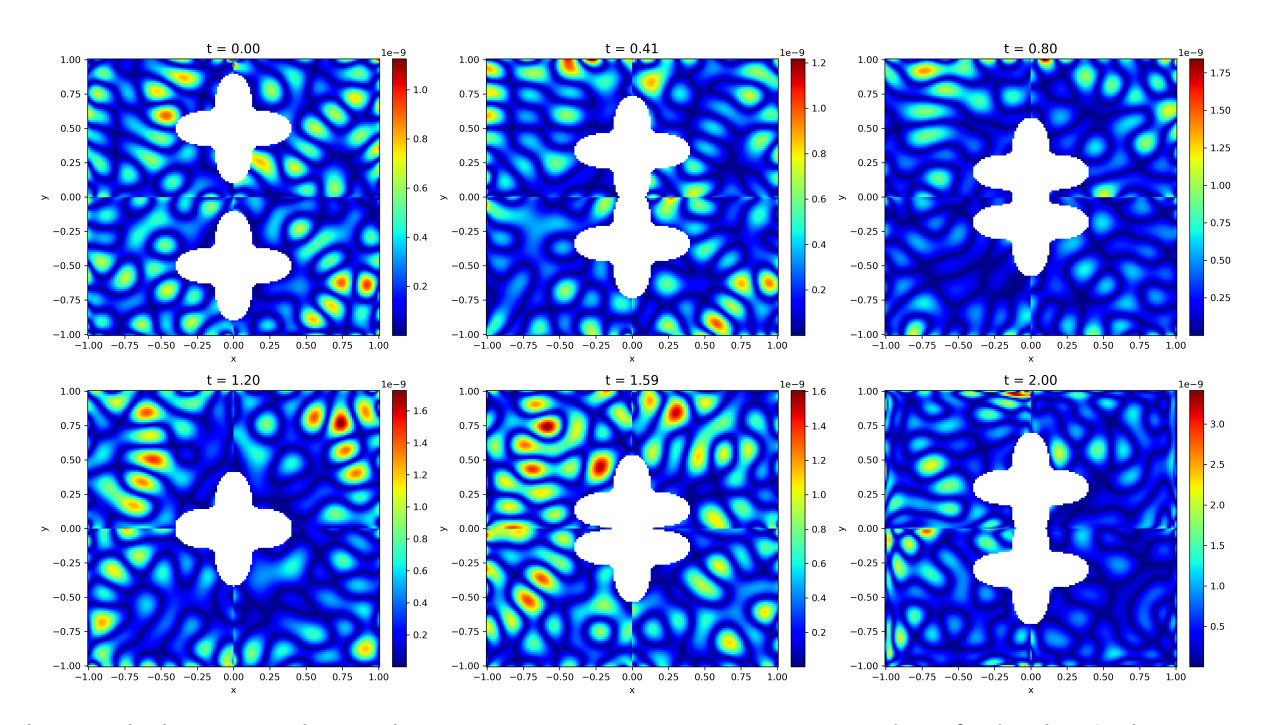


Figure 4: Absolute error on the spatial cross-sections at t = 0, 0.41, 0.80, 1.20, 1.59, and 2.00 for the Klein-Gordon equation (6.7)

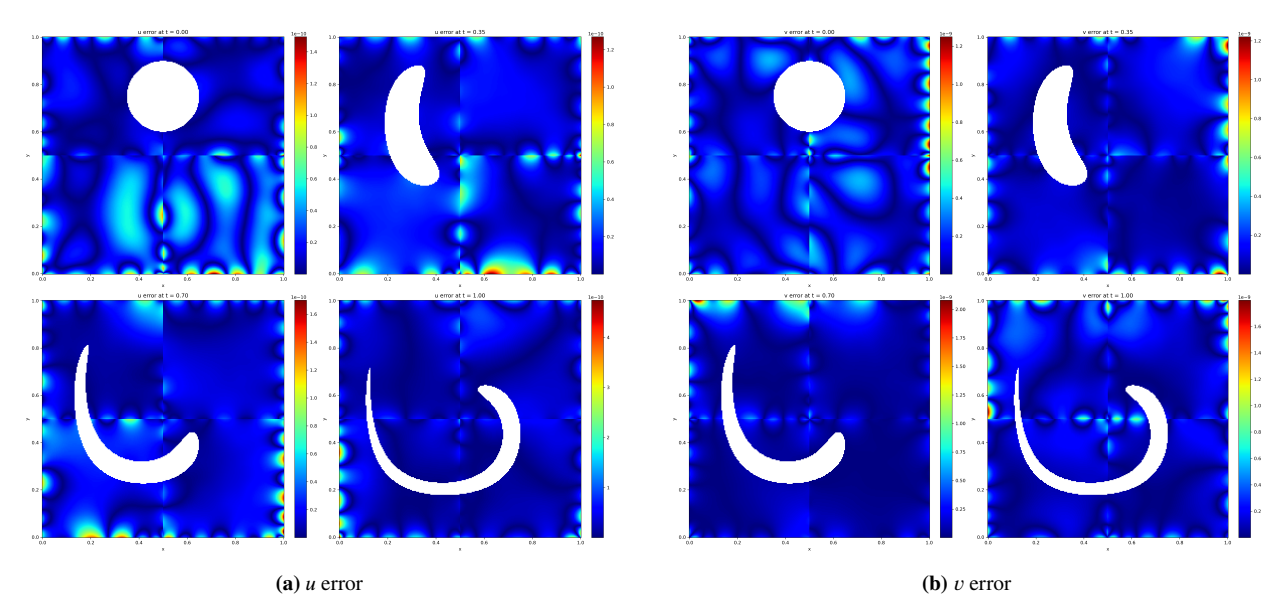


Figure 5: Absolute errors of u and v at different time instances t = 0, 0.35, 0.70, 1.00. The white region indicates the moving hole $\Omega(t)$ transported by the prescribed velocity field.

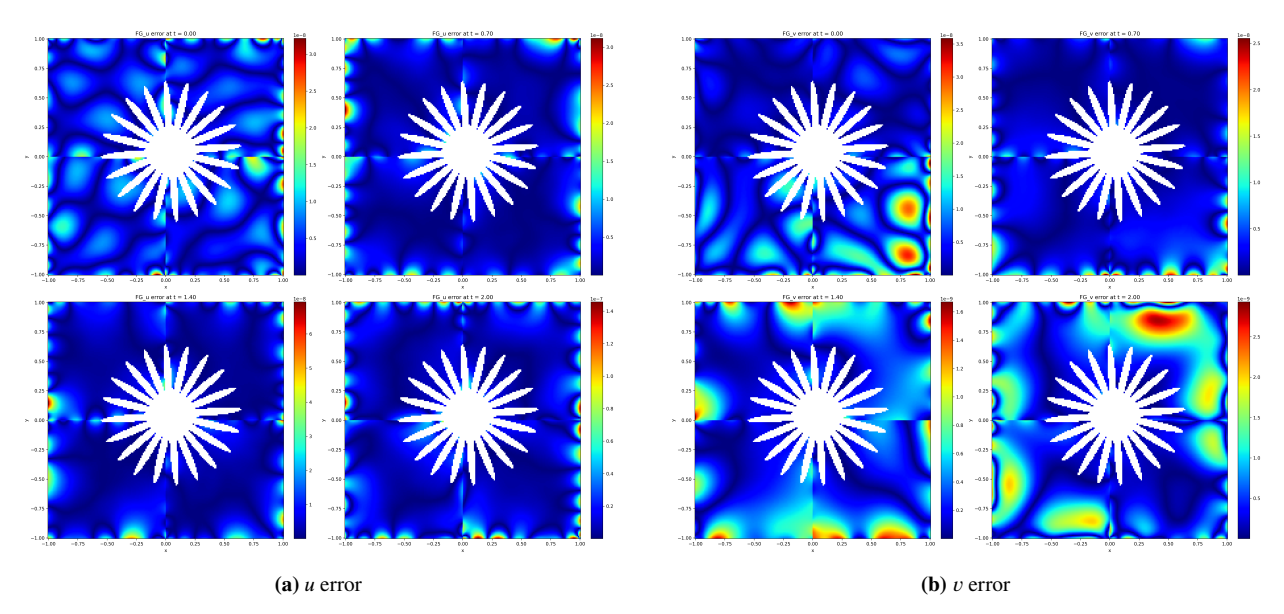


Figure 6: Absolute errors of u and v at different time instances t = 0, 0.49, 1.00, 2.00.

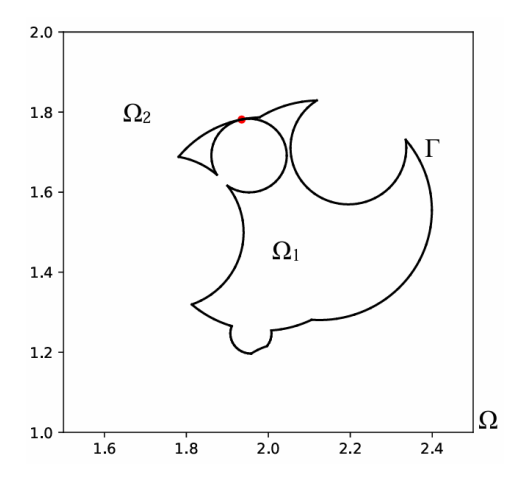


Figure 7: A two-dimensional complex geometry.

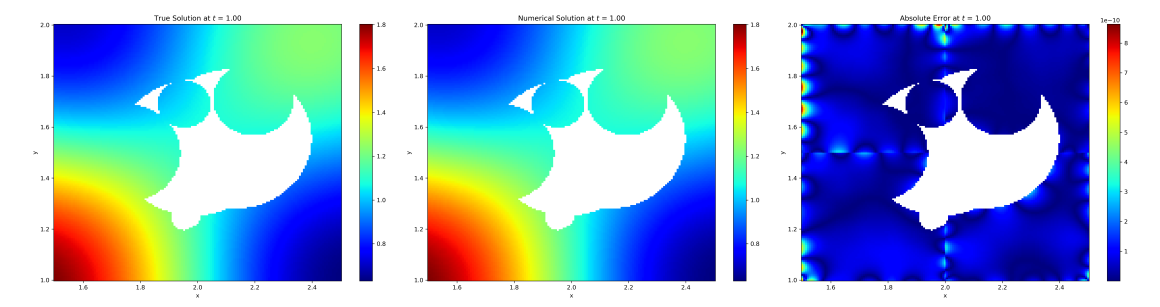


Figure 8: True solution (left), numerical solution (middle), and absolute error (right) at the final time t = 1.00 for the nonlinear diffusion equation (6.12).

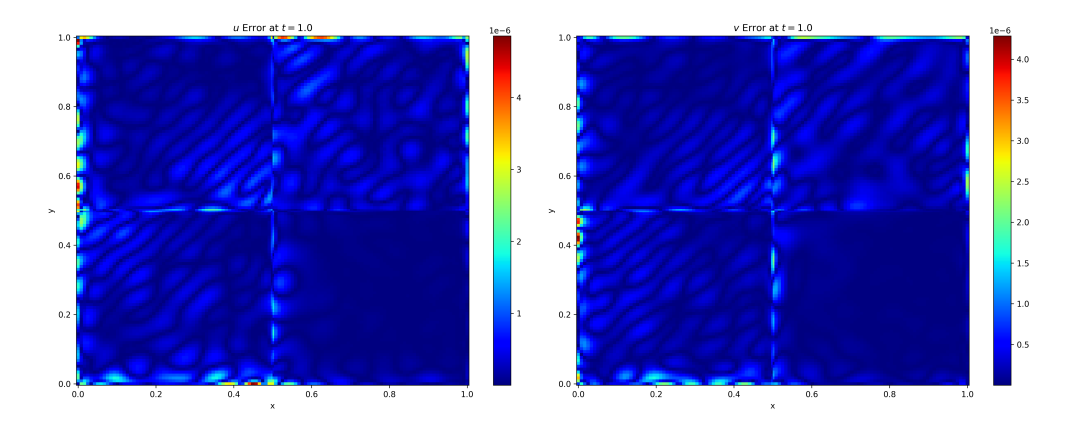


Figure 9: Absolute errors of u (left) and v (right) at the final time t = 1.00 for the Burgers equations (A.5).